Astronomy & Astrophysics

Black hole virial masses from single-epoch photometry

The miniJPAS test case

J. Chaves-Montero[1]⬤, S. Bonoli[1,2], B. Trakhtenbrot[3], A. Fernández-Centeno[4], C. Queiroz[5,6], L. A. Díaz-García[7],
R. M. González Delgado[7], A. Hernán-Caballero[8], C. Hernández-Monteagudo[9,10], C. Lópen-Sanjuan[11],
R. Overzier[12,13], D. Sobral[14], L. R. Abramo[6], J. Alcaniz[5,12], N. Benitez[7], S. Carneiro[15], A. J. Cenarro[11],
D. Cristóbal-Hornillos[8], R. A. Dupke[12,16,17], A. Ederoclite[8], A. Marín-Franch[11], C. Mendes de Oliveira[13],
M. Moles[7,8], L. Sodré Jr.[13], K. Taylor[18], J. Varela[11], H. Vázquez Ramió[11], and T. Civera[8]

(Affiliations can be found after the references)

ABSTRACT

Context. Precise measurements of black hole masses are essential to understanding the coevolution of these sources and their host galaxies.
Aims. We develop a novel approach for computing black hole virial masses using measurements of continuum luminosities and emission line widths from partially overlapping, narrow-band observations of quasars; we refer to this technique as single-epoch photometry.
Methods. This novel method relies on forward-modelling quasar observations for estimating emission line widths, which enables unbiased measurements even for lines coarsely resolved by narrow-band data. We assess the performance of this technique using quasars from the Sloan Digital Sky Survey (SDSS) observed by the miniJPAS survey, a proof-of-concept project of the Javalambre Physics of the Accelerating Universe Astrophysical Survey (J-PAS) collaboration covering ≃1 deg^2 of the northern sky using the 56 J-PAS narrow-band filters.
Results. We find remarkable agreement between black hole masses from single-epoch SDSS spectra and single-epoch miniJPAS photometry, with no systematic difference between these and a scatter ranging from 0.4 to 0.07 dex for masses from $\log(M_{BH}) \simeq 8$ to 9.75, respectively. Reverberation mapping studies show that single-epoch masses present approximately 0.4 dex precision, letting us conclude that our novel technique delivers black hole masses with only mildly lower precision than single-epoch spectroscopy.
Conclusions. The J-PAS survey will soon start observing thousands of square degrees without any source preselection other than the photometric depth in the detection band, and thus single-epoch photometry has the potential to provide details on the physical properties of quasar populations that do not satisfy the preselection criteria of previous spectroscopic surveys.

Key words. galaxies: active – galaxies: photometry – quasars: emission lines – line: profiles

1. Introduction

Quasars are the most luminous persistent sources known; as a result, they enable us to study the Universe from late to very early epochs (e.g. Fan et al. 2006; Mortlock et al. 2011; Bañados et al. 2018; Yang et al. 2020a; Wang et al. 2021). For example, quasars are excellent large-scale structure tracers at redshifts where the number density of bright galaxies is too low for statistical studies (e.g. Busca et al. 2013; Castorina et al. 2019; Hou et al. 2021), provide crucial information about the re-ionisation history of the Universe (e.g. Miralda-Escudé 1998; Fan et al. 2006; Bañados et al. 2018; Davies et al. 2018; Wang et al. 2020; Yang et al. 2020b), and have been proposed as standardisable candles (e.g. Watson et al. 2011; Wang et al. 2014; Risaliti & Lusso 2019), which provides a new avenue to extending Hubble parameter constraints towards high redshift.

The accepted physical picture is that a quasar is powered by the accretion of matter onto a supermassive black hole (SMBH; e.g. Hoyle & Fowler 1963; Salpeter 1964; Lynden-Bell 1969), which is inferred to exist at the centre of every massive galaxy (e.g. Kormendy & Richstone 1995; Magorrian et al. 1998; Ferrarese & Merritt 2000). The discovery of correlations between multiple galaxy properties and SMBH mass (e.g. Magorrian et al. 1998; Ferrarese & Merritt 2000; Gebhardt et al. 2000; Gültekin et al. 2009; Kormendy & Ho 2013; McConnell

& Ma 2013) suggests a coevolution between SMBHs and their host galaxies, during which the energy released by the accreting SMBH self-regulates its growth and impacts the evolution of its host (Silk & Rees 1998; King 2003; Di Matteo et al. 2005). The coevolution scenario is also supported by the similar redshift evolution of the cosmic SMBH accretion rate and the cosmic star formation rate up to $z = 4$ (Merloni et al. 2004; Silverman et al. 2008; Shankar et al. 2009; Aird et al. 2010; Delvecchio et al. 2014; Yang et al. 2018) as well as the need for active galactic nucleus feedback to explain the stellar-to-halo mass relation for massive galaxies in hydrodynamical simulations and semi-analytic models (e.g. Croton et al. 2006; Somerville et al. 2008; Dubois et al. 2012; Sijacki et al. 2015; Schaye et al. 2015; Weinberger et al. 2017; Pillepich et al. 2018). However, the nature of the SMBH-galaxy relation is still not completely understood; for instance, the presence of SMBHs with masses larger than 10^9 $M_\odot$ at $z > 6$ raises an important question about the origin and fast growth of these objects (see Inayoshi et al. 2020, for a recent review).

In the local universe, SMBH masses are estimated by resolving the dynamics of stars (e.g. Tremaine et al. 2002; Marconi & Hunt 2003; Davies et al. 2006; Onken et al. 2007) or gas (e.g. Davies et al. 2004a,b; Hicks & Malkan 2008) within the SMBH's gravitational sphere of influence. At cosmological distances, spatially resolving this region is impossible, and the

standard approach to estimating SMBH masses for distant galaxies relies on measurements of the virial motion of gas in the broad-line region (BLR; e.g. Czerny & Hryniewicz 2011). The most precise method for computing virial masses is reverberation mapping (RM; e.g. Blandford & McKee 1982; Peterson 1993; Netzer & Peterson 1997), which yields robust SMBH mass estimates consistent with dynamical masses (e.g. Bentz et al. 2013). Reverberation mapping measures the velocity of clouds in the BLR from the width of broad emission lines and the BLR size from the time lag between the continuum and emission line variability; to do so, it requires multiple spectroscopic observations over an extended period of time at high cadence (e.g. MacLeod et al. 2010; Bentz et al. 2013), which has limited the application of this technique to a few hundred sources so far (Kaspi et al. 2021).

The only method for estimating SMBH virial masses for a large number of sources is single-epoch spectroscopy (SES; e.g. Wandel et al. 1999; McLure & Jarvis 2002; Vestergaard 2002), which relies on the tight correlation between quasar continuum luminosity and BLR size (e.g. Kaspi et al. 2000, 2005; Bentz et al. 2006, 2009, 2013; Lira et al. 2018) to compute SMBH masses from a single spectrum. These lesser requirements translate into noisier SMBH mass estimates compared to RM, which require empirical calibration either from RM (e.g. Kaspi et al. 2000, 2005; Bentz et al. 2013) or internally based on the availability of multiple emission lines for the same object (e.g. McLure & Jarvis 2002; Vestergaard & Peterson 2006; Shen et al. 2011). Taken together with the systematics involved in the measurement of line widths, these sources of uncertainty result in differences between SMBH masses from SES and RM as large as 0.5 dex (e.g. McLure & Jarvis 2002; Vestergaard & Peterson 2006; Shen 2013; Peterson 2014).

Traditionally, measuring SMBH masses was a prerogative of spectroscopic surveys because the spectral resolution of photometric surveys was too coarse to resolve even the broadest quasar emission lines, which present widths of thousands of $km\,s^{-1}$. In addition, photometric redshifts from broadband photometry do not present enough precision for unambiguous line identification. The emergence of medium- and narrow-band photometric surveys continuously covering a large wavelength range, such as the Subaru Cosmic Evolution Survey 20 (Subaru COSMOS 20; Taniguchi et al. 2015; Sobral et al. 2018), the Advance Large Homogeneous Area Medium Band Redshift Astronomical (ALHAMBRA) survey (Moles et al. 2008), the National Optical Astronomy Observatory (NOAO) Extremely Wide-Field Infrared Imager (NEWFIRM) Medium-Band Survey (NMBS; van Dokkum et al. 2009), the Survey for High-z Absorption Red and Dead Sources (SHARDS; Pérez-González et al. 2013), the Physics of the Accelerating Universe Survey (PAUS; Eriksen et al. 2019), and the Javalambre-Physics of the Accelerating Universe Astrophysical Survey (J-PAS; Benitez et al. 2014), is progressively changing this picture. Multi-band photometric surveys have reached high enough spectral resolution to first detect broad emission lines (Chaves-Montero et al. 2017; Lumbreras-Calle et al. 2019) and then detect narrow lines and approximately resolve the profile of broad lines (Alarcon et al. 2021; Bonoli et al. 2021; Martínez-Solaeche et al. 2021).

In this work, we develop the first method for measuring SMBH virial masses from narrow-band 'photospectra', photometric observations from a contiguous set of partially overlapping narrow-band filters. This technique estimates the virial velocity of BLR clouds from the width of broad emission lines and the size of the BLR from the continuum luminosity; given the similarity of this technique with SES, we dub this approach

single-epoch photometry (SEP). We show that the resolution of J-PAS photospectra is too coarse for backward-modelling[1] emission line widths in an unbiased fashion; motivated by this, we combine forward-modelling quasar observations and Bayesian inference to measure continuum luminosities and emission line widths. To validate our methodology, we use 54 Sloan Digital Sky Survey (SDSS; York et al. 2000) quasars observed by the miniJPAS survey (Bonoli et al. 2021), a proof-of-concept project of the J-PAS collaboration. By comparing SES masses from SDSS and SEP masses from miniJPAS, we find that SEP delivers unbiased SMBH mass estimates with only slightly less precision than SES measurements for most masses. Our findings open up the possibility of studying the physical properties of quasar populations that do not satisfy the preselection criteria of previous spectroscopic surveys but will be observed by future narrow-band surveys such as J-PAS.

The paper is organised as follows. In Sect. 2 we introduce the dataset that we use to calibrate the performance SEP. In Sect. 3 we describe our approach to measuring continuum luminosities, emission line properties, and SMBH virial masses from narrow-band data, and in Sect. 4 we use SDSS quasars observed by the miniJPAS survey to estimate the precision of the previous measurements. In Sect. 5 we summarise our main findings and conclude.

Throughout this paper we consider *Planck* 2015 cosmological parameters (Planck Collaboration VI 2014): $\Omega_m = 0.314$, $\Omega_\Lambda = 0.686$, $\Omega_b = 0.049$, $\sigma_8 = 0.83$, $h = 0.67$, and $n_s = 0.96$. We use the term quasar to refer to unobscured active galactic nuclei with at least one emission line broader than $1000\,km\,s^{-1}$. Emission lines with central wavelengths smaller and larger than $\lambda = 2000\,Å$ are provided in vacuum and air wavelengths, respectively. All magnitudes are reported in the AB system (Oke & Gunn 1983). We use the symbol log to indicate decimal logarithms.

2. Data

2.1. Narrow-band data: miniJPAS

The miniJPAS survey (Bonoli et al. 2021) observed $\simeq 1\,deg^2$ of the northern sky using the J-PAS filter system, which includes 54 partially overlapping narrow-band filters of full width at half maximum (FWHM) $\simeq 145\,Å$ covering the optical range from 3780 to 9100 Å and 2 broader filters expanding over the UV and the near-infrared up to approximately 3100 and 10 000 Å, respectively. The observations were carried out using an interim camera mounted on the 2.5 m diameter Javalambre Survey Telescope at the Astrophysical Observatory of Javalambre, which will be the same telescope conducting observations for the J-PAS survey. This survey was designed to serve as a proof-of-concept for the J-PAS project (Benitez et al. 2014).

The footprint of miniJPAS covers the Extended Groth Strip (EGS) field partially, where ancillary data from the All-Wavelength EGS International Survey (AEGIS; Davis et al. 2007) and SDSS (York et al. 2000) are publicly available. To facilitate the comparison with other surveys, each pointing of miniJPAS was observed not only with all J-PAS filters, but also with the broadband filters u, g, r, and i. The depth of miniJPAS

---

[1] Backward-modelling refers to the process of measuring some target property directly from observations, while forward-modelling indicates the process of first producing plausible values of such a property using a theoretical model, and then measuring it by comparing these values with observations.

in a circular aperture of 3″ diameter reaches $m \simeq 22-23.5$ AB at 5σ for the 54 narrow-band filters and up to $m = 24$ AB for the broader filters. The primary catalogue of this survey contains more than 64 000 sources detected in the r band with matched forced photometry in all other bands (see Bonoli et al. 2021, for more details).

The J-PAS filter system[2] (Brauneck et al. 2018a,b) was designed to provide accurate photometric redshifts for both blue and red galaxies up to $z \sim 1$ (Benítez et al. 2009; Benitez et al. 2014), and for quasars up to $z \simeq 6$ (Abramo et al. 2012; Chaves-Montero et al. 2017). The first results from miniJ-PAS confirmed the expectations of sub-percent photo-z precision (Bonoli et al. 2021; Hernán-Caballero et al. 2021), the potential of the J-PAS filter system to detect and characterise emission line sources (Bonoli et al. 2021; González Delgado et al. 2021; Martínez-Solaeche et al. 2021), and more specifically to capture the main features of low redshift quasars (Bonoli et al. 2021) using QSFIT (Calderone et al. 2017). Furthermore, the *William Herschel* Telescope (WHT) Enhanced Area Velocity Explorer (WEAVE) Quasi-Stellar Object (WEAVE-QSO) survey (Pieri et al. 2016) will follow up with high spectral resolution $\sim 400k$ J-PAS quasars at $z > 2$, allowing our approach to be tested and calibrated further.

2.2. Spectroscopic data: SDSS

The SDSS survey (York et al. 2000) also observed the EGS field, and thus we can use quasars with SES measurements from SDSS to estimate the performance of SEP for miniJPAS. In this section we describe the main characteristics of the SDSS data we use.

To validate our methodology, we use publicly available SES measurements from the 14th data release of the SDSS quasar value-added catalogue (SDSS14Q; Rakshit et al. 2020), which contains 526 356 sources observed by any of the stages of the SDSS survey up to and including this data release (York et al. 2000; Eisenstein et al. 2011; Dawson et al. 2013, 2016). Quasars included in this catalogue satisfy two selection criteria: i-band absolute magnitude brighter than $M_i(z = 2) = -20.5$ and at least one emission line broader than $FWHM = 500\,\mathrm{km\,s^{-1}}$. For each source, the SDSS14Q catalogue includes the most robust spectroscopic redshift solution from SDSS (see Pâris et al. 2018), the FWHM and equivalent width (EW) of the broadest emission lines, the monochromatic continuum luminosity nearby these lines, and SMBH virial mass estimates based on these key spectroscopic measurements. The spectral information was measured using the publicly available multi-component spectral fitting code PYQSOFIT[3] (Guo et al. 2018), which uses multiple components to model the continuum emission and emission lines of each quasar separately (for a detailed description of the code and its applications see Guo et al. 2019; Shen et al. 2019).

2.3. Validation sample

We generate the quasar validation sample by cross-matching miniJPAS observations and the 12th data release of the SDSS quasar superset catalogue (SDSS12Q, Pâris et al. 2017), which contains visually inspected spectra and redshifts from any of the stages of the SDSS survey up to and including this data release. We find that miniJPAS observed 117 SDSS quasars and that

85 out of these present successful SES measurements from the SDSS14Q catalogue.

We generate a photospectrum for each source by combining 3″ aperture magnitudes from each of the miniJPAS narrow-band filters. We use this type of magnitude due to the point-like nature of quasars, and we correct aperture to total magnitudes following a two-step procedure. First, we compute the median difference between 3″ aperture magnitudes of bright, unsaturated stars from each miniJPAS tile and point spread function magnitudes from the Panoramic Survey Telescope and Rapid Response System 1 (Pan-STARRS1; Chambers et al. 2016). We use these offsets to correct the magnitudes of each tile separately, and then we compute the median difference between the resulting magnitudes and synthetic magnitudes obtained by convolving the spectra of 115 stars from the SDSS12Q catalogue with the J-PAS filter system. Finally, we apply these differences to the partially corrected magnitudes. We note that this two-step approach corrects for both the finite size of 3″ apertures and spectral offsets (for more details about this process, see Queiroz et al., in prep.).

The miniJPAS survey conducted observations of most filters between May and October of 2018, and of a few filters in July 2019 (Bonoli et al. 2021). Due to the variable nature of quasars, we could expect variability to manifest as artificial emission or absorption lines in miniJPAS photospectra due to filters observed at different epochs. The impact of variability is increasingly weak for more luminous quasars (e.g. Hook et al. 1994; MacLeod et al. 2012; Meusinger & Weiss 2013; Kozłowski et al. 2016; Caplar et al. 2017), and the expected level of optical variability is ~ 0.1 AB per 100 rest-frame days for the faintest sources. The maximum time span between miniJPAS observations is approximately 400 days, so we expect the largest band-to-band magnitude fluctuations to be smaller than 0.2 and 0.1 AB for quasars at $z = 1$ and 3, respectively. Taken together with the high luminosity of miniJPAS quasars (see Sect. 4.1), we expect minimal impact of variability on miniJPAS observations. On the other hand, the difference between SDSS and mini-JPAS observations is of the order of years for some sources, and thus we expect variability to affect the comparison between SES and SEP measurements. We note that the virial theorem suggests that a change of X dex in continuum luminosity manifests as a $-0.25\,X$ dex difference in FWHM.

In the top panel of Fig. 1, we display the median spectral signal-to-noise ratio (S/N) of the 85 SDSS quasars with successful SES measurements as a function of their miniJPAS r-band magnitude. Blue, orange, and green dots indicate the results for sources with $r < 20$, $20 < r < 21$, and $21 < r < 22$, respectively. As we can see, most sources with r-band magnitude fainter than $r = 21$ present an SDSS spectrum with median S/N smaller than 4. Multiple authors have investigated the impact of S/N on the robustness of SES measurements (e.g. Shen et al. 2011, 2019; Denney et al. 2016), finding that the precision of SES masses decreases rapidly with the median S/N of SDSS spectra, reaching measurement-related errors of 0.3 dex or larger for $S/N < 10$ (e.g. Shen et al. 2011; Rakshit et al. 2020). To reduce the impact of noisy SES measurements on our analysis, in Sect. 4 we validate SEP using the 54 sources brighter than $r = 21$.

In the bottom panel of Fig. 1, we display the redshift distribution of these 54 quasars. As we can see, these sources present spectroscopic redshifts between $z \simeq 0.5$ and 3.5, which enables SEP to be tested using the lines Hβ, Mg II, and C IV. The maximum redshift for quasar detection in J-PAS is $z \simeq 6$; nonetheless, the validation sample does not present any source above $z = 4$ because the miniJPAS survey only observed $\simeq 1\,\mathrm{deg}^2$ and the

---
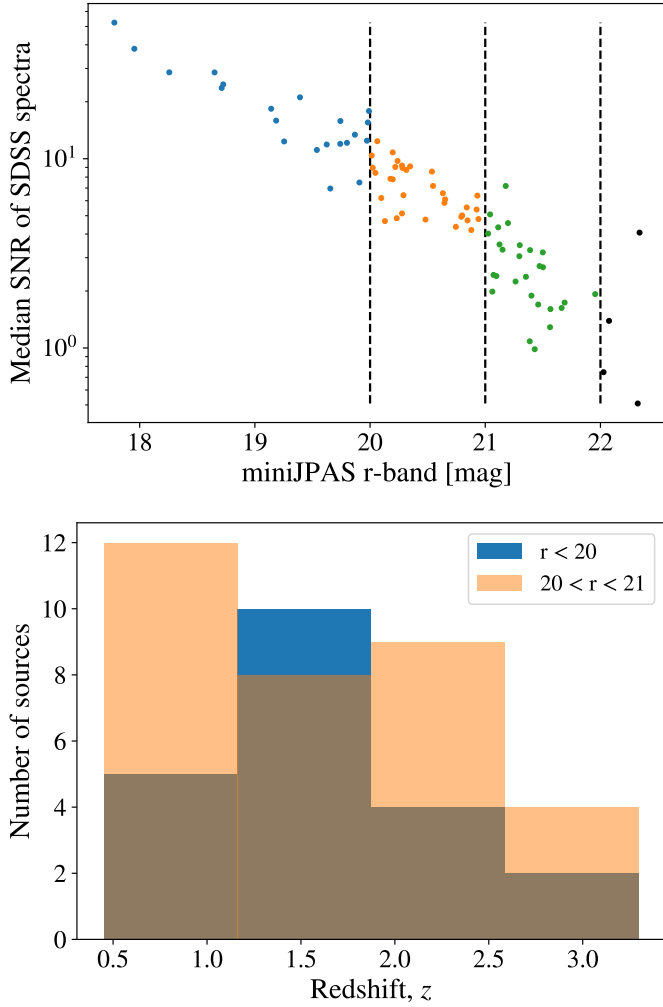
Fig. 1. Properties of SDSS quasars with successful SES measurements observed by miniJPAS. Blue, orange, and green colours indicate the results for sources with $r < 20$, $20 < r < 21$, and $21 < r < 22$, respectively. The top panel shows the median S/N of SDSS spectra as a function of miniJPAS r-band magnitude, and the bottom panel displays the redshift distribution of quasars brighter than $r = 21$.

angular number density of quasars brighter than $r = 21$ at $z > 4$ is smaller than one per square degree (Palanque-Delabrouille et al. 2013, 2016). Throughout this work, we use SDSS redshift estimates to conduct SEP measurements; however, we will not have access to spectroscopic redshifts for the majority of sources that the J-PAS survey will observe. We expect photometric redshifts with subpercent precision for J-PAS quasars (Abramo et al. 2012; Chaves-Montero et al. 2017; Bonoli et al. 2021); as a result, photometric redshift errors are expected to be a subdominant source of uncertainty for our technique (see Appendix B).

3. Model

In this section we describe our novel approach to measure SMBH masses from SEP. We first discuss the theoretical foundations of this method in Sect. 3.1, and then we describe our strategy to measure continuum luminosities, emission line properties, and SMBH masses in Sects. 3.2–3.4, respectively. Lastly, we test our methodology using simulated J-PAS photospectra in Sect. 3.5.

3.1. Theory preambles

The standard approach to measure SMBH masses at cosmological distances relies on measurements of the virial motion of gas in the BLR. Assuming that the SMBH's gravitational field dominates the motion of these clouds, we can compute SMBH masses using the virial theorem (e.g. Ho 1999; Wandel et al. 1999):

$$M_{\rm BH} = f \frac{R_{\rm BLR}(\Delta V)^2}{G}, \qquad (1)$$

where G is the gravitational constant, $R_{\rm BLR}$ indicates the size of the BLR, ΔV refers to the virial velocity of the BLR gas, and f is a dimensionless parameter of order unity that depends on the geometry, kinematics, and inclination of the BLR (see Mejía-Restrepo et al. 2018; Williams et al. 2018, and references therein). In practice, it is standard to estimate the virial velocity using either the FWHM or the dispersion of broad emission lines, each of which presents different advantages and disadvantages (e.g. Shen 2013). Throughout the remainder of this section we describe a new method to measure SMBH masses from J-PAS photospectra by leveraging the tight correlation between continuum luminosity and BLR size.

3.2. Continuum emission

The size of the BLR region presents a tight correlation with the luminosity of the quasar continuum emission, which is emitted by material in the accretion disk of the SMBH (Abramowicz & Fragile 2013) and it is compatible with a power law from the optical to the near-UV (e.g. Cristiani & Vio 1990; Vanden Berk et al. 2001). However, measuring the luminosity of the continuum is not straightforward; this is because the apparent continuum of a quasar results from the combination of the power-law continuum and other contributions such as unresolved emission and absorption lines, blended iron lines (e.g. Véron-Cetty et al. 2004), Balmer continuum emission (e.g. Wills et al. 1985), host-galaxy contamination (especially for faint sources; e.g. Shen et al. 2011; Hernán-Caballero et al. 2016), dust reddening (e.g. Hopkins et al. 2004), and photometric errors. To alleviate the impact of these features on measurements of the monochromatic continuum luminosity, we first fit a power-law model to the apparent continuum emission, and then we measure the monochromatic luminosity from the best-fitting model.

To estimate the power-law continuum, we start by selecting a set of rest-frame wavelengths λ_w not presenting strong emission features in their surroundings and sampling observer-frame photospectra in a sufficiently dense fashion up to $z = 5$. We find that the wavelengths $\lambda_w = 1350, 1700, 1800, 2200, 3100, 4000, 4200,$ and 5200 Å satisfy both criteria: these wavelengths present a separation of at least 100 Å from strong emission lines according to quasar composite spectra (e.g. Vanden Berk et al. 2001) and at least two λ_w fall within the J-PAS wavelength range up to $z \simeq 5$. We continue by identifying the J-PAS narrow band with the closest pivot wavelength[4] to the observer-frame value of each λ_w for every source. Then, we compute the median flux of each selected band and those immediately preceding and succeeding; the resulting values approximate the continuum emission. We note that this approach is largely insensitive to redshift errors perturbing λ_w less than half the width of survey filters (see Appendix B).

Even though the selected λ_w are not close to strong emission features, we find it necessary to apply some corrections

---

[4] As defined in Eq. (A.11) of Tokunaga & Vacca (2005).
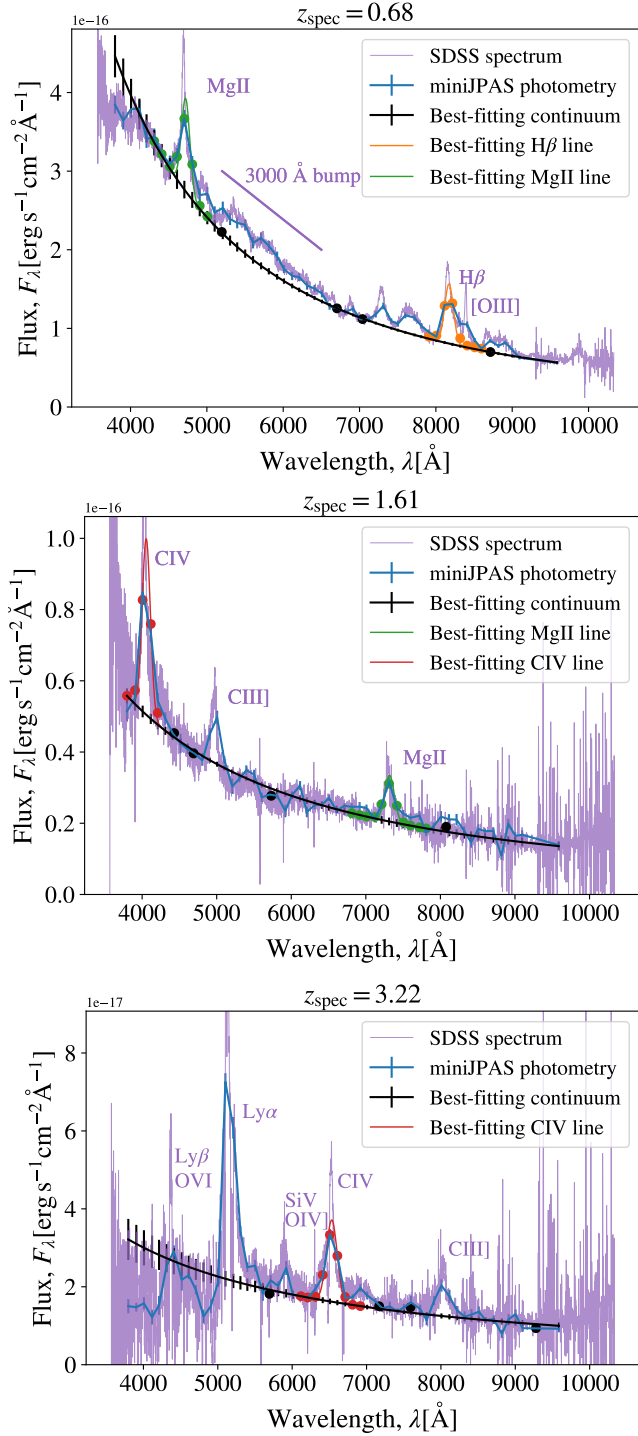
Fig. 2. Photometric decomposition of miniJPAS data from three SDSS quasars. *Top, middle*, and *bottom panels*: results for a quasar at low, intermediate, and high redshift, respectively. Blue and purple lines show miniJPAS photospectra and SDSS spectra, respectively, black lines display best-fitting continua, and orange, green, and red lines denote best-fitting Hβ, Mg II, and C IV emission lines. Error bars show 1σ-equivalent uncertainties. Despite the limited spectral resolution of J-PAS filters, we can readily see that best-fitting lines precisely capture the broad component of quasar emission lines in SDSS spectra.

to account for the impact of spectral features biasing high the continuum emission. By comparing SDSS spectra and mini-JPAS photospectra, we find that the impact of the O IV]–

Si IV $\lambda\lambda$1397.2, 1402.8 complex and blends of Fe II line emission redwards of the Mg II line is alleviated on average by reducing 10% the flux at $\lambda_w = 1350$ and 3100 Å, respectively. Furthermore, we find that reducing 10% the flux at $\lambda_w = 5200$ Å partially corrects for the change in the continuum slope starting at $\lambda \simeq 5000$ Å, which is caused by a combination of host-galaxy contamination and emission from hot dust (see Vanden Berk et al. 2001, and references therein). Both corrections enable a better estimation of the quasar continuum emission from the optical to the near-UV. On the other hand, we do not explicitly correct the quasar continuum for the impact of host-galaxy contamination because the quasars in the validation catalogue are brighter than $r = 21$ and present redshift higher than $z = 0.5$ (see Sect. 2.3), and the host-galaxy emission is increasingly weaker for brighter sources at higher redshift (e.g. Shen et al. 2011). We note that the results are weakly sensitive to all these corrections because we use multiple λ_w to estimate the continuum emission for each source.

We use the publicly available affine invariant Markov chain Monte Carlo (MCMC) ensemble sampler EMCEE (Foreman-Mackey et al. 2013)[5] to compute the best-fitting power-law model to the continuum of each source, $f_{\rm cont} = f_0 \lambda^{\alpha_\lambda}$, where f_0 and α_λ are the normalisation and spectral index of the power law, respectively. This process works as follows. For each step of the Markov chain, EMCEE draws a new value of the previous two parameters, convolves the resulting continuum with the J-PAS filter system, and compares the simulated and actual continuum emission to obtain the likelihood of the selected parameters. We ran the code using 100 independent chains of 150 steps, a burn-in phase of 75 steps, and broad uniform priors ($\alpha_\lambda \in [-3.5, 3.5]$). We verify that this configuration results in a robust sampling of the posterior. To determine the best-fitting monochromatic continuum luminosity at a particular wavelength and its error, we first compute the luminosity of the continuum at such a wavelength from every accepted step of the MCMC chains. Then, we obtain the best-fitting solution and its uncertainty by computing the median and semi-amplitude of the range enclosing the 16 and 84th percentiles of the resulting values, respectively.

In top, middle, and bottom panels of Fig. 2, we display the photometric decomposition of miniJPAS data from three SDSS quasars at $z = 0.68$, 1.61, and 3.22, respectively. The apparent magnitude of these sources is $r = 18.1$, 20.1, and 20.3, their SDSS ID 7339–56722–108, 7339–56722–153, and 7339–56722–147, and their miniJPAS ID 00853, 15867, and 14873. Even though the spectral resolution of narrow-band filters is not high enough to resolve narrow spectral features, we can readily see that miniJPAS photospectra resolve broad emission lines precisely.

We find that the best-fitting continua follow the SDSS-observed continua closely, particularly for wavelengths not contaminated by important spectral features. Black dots indicate the values used to compute the best-fitting continua; as explained above, we select these wavelength intervals because the strongest quasar emission lines do not contaminate their flux. On the other hand, weaker spectral features affect some of these wavelength intervals. In the top panel, the 3000 Å bump (Grandi 1982; Oke et al. 1984; Wills et al. 1985) and the change in the continuum slope near $\lambda = 5000$ Å (Vanden Berk et al. 2001) modify the flux of the black dots immediately redwards Mg II and Hβ, respectively; nevertheless, we can readily see that the

---

[5] https://emcee.readthedocs.io/en/stable/

flux corrections mentioned above alleviate the impact of these features.

3.3. Emission lines

Among all quasar emission lines, we are primarily interested in Hβ λ4861, Mg II λ2798, and C IV λ1549 because these lines present EWs large enough to significantly modify narrow-band photometry and are calibrated to compute SMBH virial masses (e.g. Kaspi et al. 2000, 2005; Vestergaard & Peterson 2006; Shen et al. 2011; Bentz et al. 2013). In addition, we can detect at least one of these lines from the local universe up to $z = 5$ using the J-PAS filter system, which enables a continuous estimation of SMBH masses up to such a redshift. In the following we describe our approach to extracting the properties of these emission lines.

For each source, we start by identifying the J-PAS bands with pivot wavelengths within the rest-frame intervals [4700, 5100] Å, [2600, 3000] Å, and [1450, 1630] Å for the analysis of Hβ, Mg II, and C IV, respectively. The widths of these intervals are $\Delta\lambda \simeq 2.5$, 4.3, and 3.5×10^4 km s^{-1}, which are wide enough to encompass the broadest quasar emission lines almost entirely (e.g. Rakshit et al. 2020). We restrict our analysis to emission lines with observer-frame central wavelength within the interval [4000, 8900] Å to ensure correct sampling of line wings. Then, we compute the relative difference between the miniJPAS photometry and best-fitting continuum emission for the selected bands (see Sect. 3.2), producing a line-only spectrum.

Spectral decomposition methods usually consider multiple broad and narrow components to recover the shape of emission line profiles more precisely (e.g. Greene & Ho 2005; Shen et al. 2011; Guo et al. 2019). However, to avoid degeneracies between different components due to the limited spectral resolution of J-PAS photospectra, we use a single Gaussian to compute the amplitude, centre, and width of each emission line from the line-only spectrum. We do so using the MCMC sampler EMCEE (see also Sect. 3.2): for each step of the Markov chain, EMCEE draws a new value for the amplitude, centre, and width of the target emission line, convolves the resulting line with the J-PAS filter system, and compares the simulated line and the line-only spectrum to obtain the likelihood of the selected parameters. For each line, we ran the code using 75 independent chains of 500 steps, a burn-in phase of 150 steps, and broad uniform priors. Specifically, we allow the line centre to move as much as an observer-frame distance of 75 Å from the rest-frame position of the target line, which corresponds to approximately half the width of a narrow-band J-PAS filter. This wide prior in the line centre aims to accommodate for possible velocity shifts or redshift errors. We compute the best-fitting value and error of line properties following the same strategy as for the continuum luminosity in Sect. 3.2.

We find that the [O III] $\lambda\lambda$4958.9, 5006.8 complex and blended iron lines hinder the correct estimation of line properties for Hβ and Mg II, respectively. Spectral methods usually model these features; however, the spectral resolution of J-PAS is too coarse to follow this approach. By comparing SDSS spectra and miniJPAS photospectra, we find that we can mitigate the overall impact of these features on line fits by reducing 50, 50, 25, and 50% the flux of the J-PAS bands with pivot rest-frame wavelength closest to $\lambda = 2700$, 2950, 4960, and 5008 Å, respectively. The Hβ correction is essential for all sources because the spectral resolution of J-PAS bands is not high enough to

resolve Hβ and the [O III] $\lambda\lambda$4958.9, 5006.8 complex separately. The Mg II correction only improves the results for lines broader than ~8000 km s^{-1} because for narrower lines the spectral resolution of J-PAS is high enough to resolve Mg II and blended iron lines separately. Not introducing these corrections results in overestimating the width of emission lines.

In Fig. 2, we show the best-fitting emission line models to the broad lines of example quasars. By comparing the result of photometric measurements and SDSS spectra, we can readily see that best-fitting lines capture the broad component of Hβ, Mg II, and C IV precisely. This level of agreement is remarkable given the significant difference in spectral resolution between SDSS spectra and J-PAS photospectra, with average spectral resolutions of $R \simeq 1800$ and 60 (respectively; York et al. 2000; Benitez et al. 2014). The spectral resolution of J-PAS photospectra suggests that we can only resolve lines broader than ~5000 km s^{-1}; however, this calculation does not account for the overlapping of the transmission curve of adjacent J-PAS filters.

3.4. SMBH virial masses

At cosmological distances, the standard approach to compute SMBH masses assumes that the BLR is virialised and that the SMBH gravitational field dominates the motion of gas clouds in this region. Single-epoch spectroscopy computes virial masses by leveraging the tight correlation between continuum luminosity and BLR size (e.g. Kaspi et al. 2000; Bentz et al. 2009),

$$\log\left(\frac{M_{\rm BH}}{M_\odot}\right) = A + B\log\left(\frac{\lambda L_\lambda}{10^{44}\,{\rm erg\,s^{-1}}}\right) + 2\log\left(\frac{FWHM}{{\rm km\,s^{-1}}}\right), \quad (2)$$

where FWHM stands for the full width at half maximum of broad emission lines, λL_λ refers to the monochromatic continuum luminosity – typically measured over a spectral region adjacent to the respective broad emission line –, and A and B are virial coefficients calibrated using either sources with both SES and RM measurements (e.g. Kaspi et al. 2000; Bentz et al. 2013) or internally based on the availability of multiple lines for the same source (e.g. McLure & Jarvis 2002; Vestergaard & Peterson 2006; Trakhtenbrot & Netzer 2012; Marinello et al. 2020). We compute Hβ-, Mg II-, and C IV-based virial masses using the continuum luminosity at $\lambda = 5100$, 3000, and 1350 Å, respectively, and the same virial coefficients as SDSS-based quasar catalogues (Shen et al. 2011; Rakshit et al. 2020): $A = 0.91$ and $B = 0.50$ for Hβ (Vestergaard & Peterson 2006), $A = 0.74$ and $B = 0.62$ for Mg II (Shen et al. 2011; Trakhtenbrot & Netzer 2012), and $A = 0.66$ and $B = 0.53$ for C IV (Vestergaard & Peterson 2006). Consequently, SMBH masses depend approximately four times more strongly on the FWHM than continuum luminosity measurements.

Different calibrations or spectral decomposition techniques may result in differences as large as 0.4 dex between RM and SES masses (e.g. Collin et al. 2006; Kelly et al. 2009; Shen 2013; Dalla Bontà et al. 2020); motivated by this, some works recalibrate virial coefficients using RM and SES measurements from the same spectral decomposition code to reduce these errors. It is also worth noting that the precision of SMBH mass estimates depends on the emission line used during the inference process: Hβ-based masses present a scatter of 0.3 and 0.5 dex relative to Mg II- and C IV-based masses, respectively (Trakhtenbrot & Netzer 2012).

To compute SEP masses, we use continuum luminosities and line widths estimated from J-PAS photospectra (see Sects. 3.2 and 3.3, respectively). Ideally, we would recalibrate Eq. (2)

coefficients using sources presenting both RM and SEP mass measurements; however, miniJPAS did not observe any quasar with RM measurements. In Sect. 4, we resort to recalibrating these coefficients using sources with both single-epoch spectroscopic and photometric measurements; to do so, we use the gradient-based BFGS algorithm (Broyden 1970; Fletcher 1970; Goldfarb 1970; Shanno & Kettler 1970) implemented in SCIPY (Virtanen et al. 2020). This recalibration has two important benefits: it absorbs systematic differences between spectroscopic and photometric measurements of both continuum luminosity, which may be caused by over- or under-estimating the correction from aperture to total magnitudes (see Sect. 2.3), and line widths, which may appear due to the different number of components used to fit line profiles (see Sect. 3.3).

3.5. Tests using idealised simulations

In order to thoroughly test our methodology, we proceed to study the feasibility of using SEP to measure SMBH masses using simulated observations of J-PAS quasars.

Modelling the spectral energy distribution of a quasar is challenging due to correlations between multiple quasar properties (e.g. Baldwin 1977; Dong et al. 2009; Shen et al. 2011), the presence of a panoply of weak and blended emission lines (e.g. Davidson & Netzer 1979), the complex profile of some broad emission lines (e.g. Nagao et al. 2006; Shen et al. 2011; Kollatschny & Zetzl 2013), the diversity of quasar continua (e.g. Jensen et al. 2016), emission line velocity shifts (e.g. Richards et al. 2011; Shen et al. 2016), and host-galaxy contamination (e.g. Vanden Berk et al. 2001). Instead of accounting for all these effects, we proceed to generate idealised quasar observations by modelling the quasar continuum emission as a power law and each broad emission line as a single Gaussian. This approach ensures that the only sources of uncertainty affecting SEP masses are the limited resolution of the J-PAS filter system and the level of photometric errors expected for this survey. In Sect. 4, we study the aggregated impact of all the aforementioned effects and others such as variability by comparing SES and SEP measurements from quasars in the miniJPAS validation sample (Sect. 2.3).

For each source, we first modelled the continuum emission using a power law of index $\alpha_\lambda = -1.56$, which provides an excellent fit to the quasar continuum emission from Lyα to Hβ (Vanden Berk et al. 2001). Then, we added the emission lines Hβ, Mg II, and C IV to the continuum emission, which we modelled using a single Gaussian function with the same width. After that, we redshifted the resulting spectral energy distribution from rest- to observer-frame, and we convolved it with the J-PAS filter system. Finally, we perturbed mock photospectra according to the level of photometric uncertainties expected for the J-PAS survey (Benitez et al. 2014). In summary, four free parameters characterise each simulated photospectra: continuum r-band magnitude, rest-frame EW, FWHM, and redshift. To generate mock observations, we first drew 10 500 random combinations of these parameters within the intervals $z \in [0.01, 4.50]$, $r \in [18, 23]$, $\log(EW/Å) \in [1, 2.6]$, and $\log(FWHM/\mathrm{km\,s^{-1}}) \in [2.5, 4.0]$ using Latin hypercube sampling (McKay et al. 1979). Then, we followed the previously mentioned strategy to generate a J-PAS photospectra for each combination of parameters.

In Fig. 3, we compare the SEP measurements from mock photospectra and the input quantities used to simulate these. We note that we analysed mock observations using a slightly modified version of the model described in Sect. 3: we did not apply any correction to either the continuum emission or emission lines
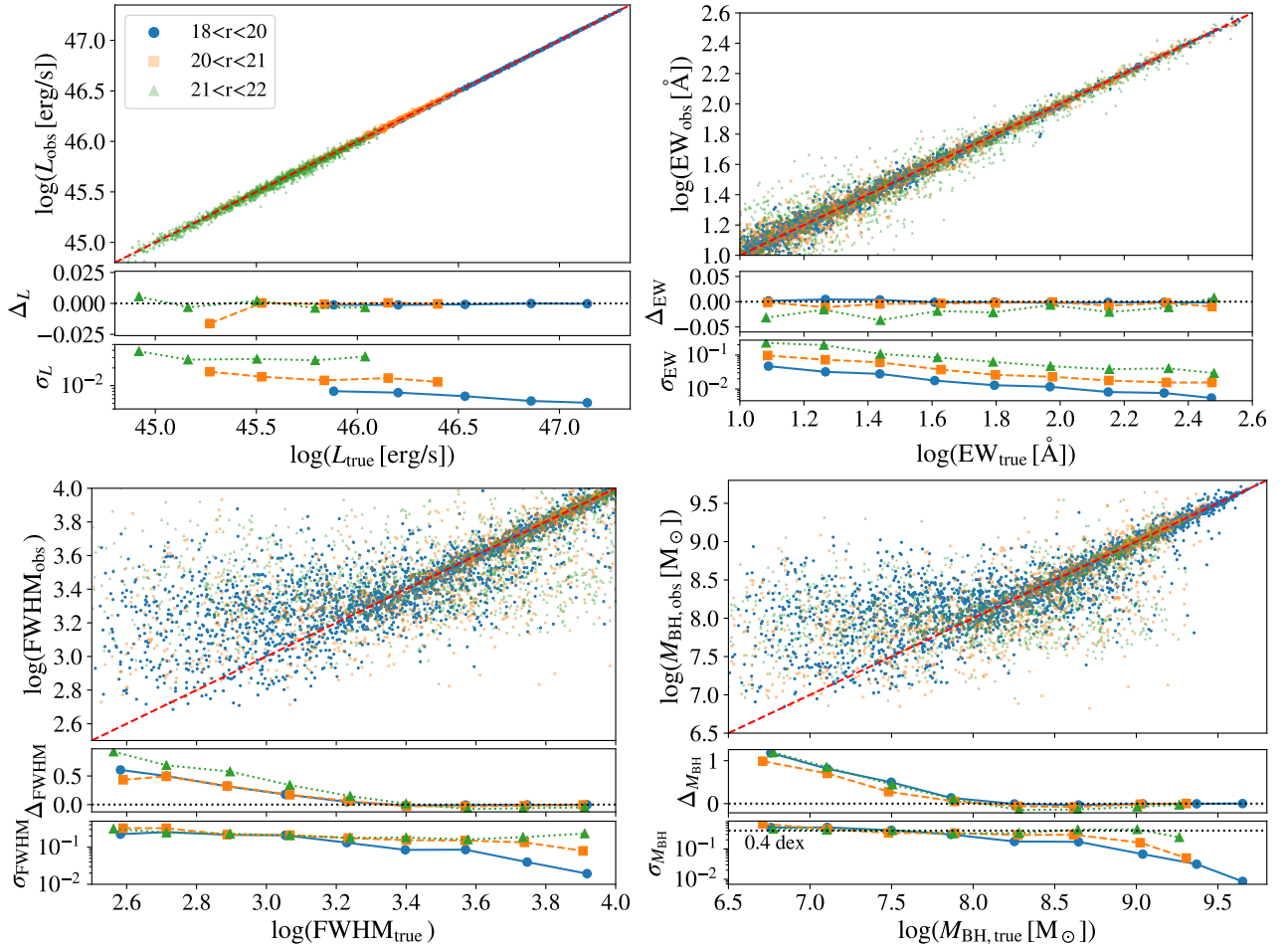
because simulated photospectra do not incorporate any contaminant. Blue dots, orange squares, and green triangles indicate the results for sources with $18 < r < 20$, $20 < r < 21$, and $21 < r < 22$, respectively, and red dashed lines indicate the 1:1 relations between input and measured quantities. In each panel, the middle and bottom sub-panels display the mean and standard deviation of the logarithmic difference between input and measured values. As expected, the precision of all measurements is increasingly larger for brighter sources as the relative impact of the associated photometric errors decreases.

In the top-left and top-right panels, we display measurements of the monochromatic continuum luminosity at 1350 Å and the EW of C IV, respectively. As we can see, the precision of the measurements increases for more luminous sources and stronger lines; this is because the relative impact of photometric errors decreases with both the brightness of the continuum and the strength of emission lines. We also find that our model only delivers unbiased measurements for sources brighter than $r \simeq 21$; motivated by this, we only consider sources brighter than such a magnitude to estimate the performance of SEP in Sect. 4.

In the bottom-left panel, we show measurements of the FWHM of C IV. We find that the precision of these measurements increases for broader lines; this is because the J-PAS filter system resolves wider lines with a larger number of bands. The most prominent feature of this panel is that FWHM measurements display a systematic bias for emission lines narrower than $\approx 1500\,\mathrm{km\,s^{-1}}$. We can understand this trend in terms of the limited spectral resolution of the J-PAS filter system: on average, emission lines narrower than $\approx 1500\,\mathrm{km\,s^{-1}}$ perturb the flux of a single J-PAS band, which causes a complete degeneracy between the amplitude and FWHM of the best-fitting line. For such lines, our method delivers practically any result between the actual width and the minimum one resolvable, thereby biasing high FWHM measurements. In Appendix A, we show that backward-modelling observations result in systematic biases even for lines as wide as $\approx 10\,000\,\mathrm{km\,s^{-1}}$; therefore, forward-modelling quasar observations enables us to push this limit by almost an order of magnitude. We note that our naive estimate for the width of the narrowest line resolvable by J-PAS is approximately three times larger than the actual value (see Sect. 3.3).

In the bottom-right panel, we display measurements of C IV-based SMBH mass. We note that we compute SMBH masses using the virial coefficients quoted in Sect. 3.4. As we can see, our method yields unbiased masses only for sources with $\log(M_{BH}/M_\odot) \gtrsim 8$, reflecting the biased FWHM measurements for lines narrower than $\simeq 1500\,\mathrm{km\,s^{-1}}$. For sources with FWHM larger than the aforementioned threshold, we find that SEP masses show no systematic bias and that the precision of these ranges from 0.4 to 0.01 dex for SMBH with masses from $\log(M_{BH}/M_\odot) \simeq 8$ to 9.75, respectively. We also find that the precision of these measurements increases with the SMBH mass for sources brighter than $r = 21$, which is explained by the increasing precision of both continuum luminosity and FWHM measurements for sources with brighter continua and broader lines. We note that we find similar results for Hβ- and Mg II-based measurements.

In Fig. 4, we display SEP mass measurements from Hβ, Mg II, and C IV as a function of redshift. As we can see, these lines enable SMBH masses from $z = 0$ to 5 to be measured continuously. We only display results for sources with an actual mass larger than $\log(M_{BH}/M_\odot) = 7.5$; we set this threshold to understand better the impact of the limited resolution of the J-PAS filter system on measurements for low mass sources. We

Fig. 3. SEP measurements of $\lambda L_\lambda(1350\,\text{\AA})$ continuum luminosity (*top-left panel*), C IV EW (*top-right panel*), C IV FWHM (*bottom-left panel*), and C IV-based SMBH mass (*bottom-right panel*) from simulated J-PAS sources. Blue dots, orange squares, and green triangles show the results for sources with $18 < r < 20$, $20 < r < 21$, and $21 < r < 22$, respectively, and dashed red lines indicate a one-to-one relation between actual and measured properties. The *middle and bottom sub-panels* display the mean and standard deviation of the logarithmic difference between actual and measured properties. We find that our method yields unbiased FWHM measurements only for lines broader than $\simeq 1500\,\text{km s}^{-1}$ due to the limited spectral resolution of J-PAS photospectra, which prevents us from measuring the mass of sources with $\log(M_{\text{BH}}/M_\odot) \lesssim 8$ in an unbiased fashion. We find similar results for Hβ and Mg II.
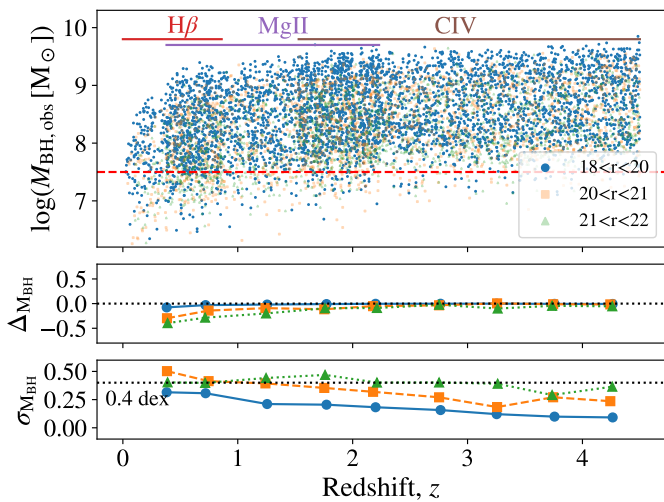
Fig. 4. SEP masses from simulated J-PAS observations of sources with actual SMBH masses larger than $\log(M_{\text{BH}}/M_\odot) = 7.5$. The dashed red line indicates this threshold. As we can see, the combination of Hβ, Mg II, and C IV enables SMBH masses from $z = 0$ to 5 to be continuously measured.

find that our model yields unbiased SMBH masses for sources with both $r < 20$ and $\log(M_{\text{BH}}/M_\odot) > 7.5$ across the whole redshift range. On the other hand, sources with $r > 20$ present slightly biased masses below $z = 1$, especially those with less massive SMBHs. This is due to the combination of two effects: the precision of SEP measurements increases with both apparent magnitude and line width, and at fixed FWHM (in km s^{-1}), the observer-frame line width (in Å) grows with redshift as $1 + z$. We check that our model yields unbiased SMBH mass estimates for sources with emission lines broader than an observer-frame width of $FWHM = 30\,\text{\AA}$.

4. Results

In Sect. 3, we describe SEP and we validate our methodology using simulated J-PAS photospectra. In this section we characterise the precision of this technique by comparing SEP and SES measurements for 54 SDSS quasars observed by the miniJPAS survey (see Sect. 2.3). In Sects. 4.1–4.3, we show the results for continuum luminosities, emission line properties, and SMBH virial masses, respectively, and we gather these in Table 1.

Table 1. SEP measurements for some sources in the miniJPAS validation catalogue.

z	$\log(L_\lambda[\mathrm{erg\,s^{-1}}])$			$\log(FWHM[\mathrm{km\,s^{-1}}])$			$\log(M_{\mathrm{BH}}[M_\odot])$		
	5100 Å	3000 Å	1350 Å	Hβ	Mg II	C IV	Hβ	Mg II	C IV
0.482	$44.16^{+0.03}_{-0.03}$	$44.23^{+0.02}_{-0.02}$	–	$3.81^{+0.29}_{-0.37}$	$3.61^{+0.52}_{-0.55}$	–	8.53 ± 0.66	7.65 ± 1.06	–
0.531	$44.10^{+0.04}_{-0.04}$	$43.86^{+0.04}_{-0.04}$	–	$3.91^{+0.15}_{-0.36}$	$3.87^{+0.18}_{-0.16}$	–	8.73 ± 0.51	7.94 ± 0.34	–
0.548	$44.32^{+0.03}_{-0.03}$	$44.29^{+0.04}_{-0.04}$	–	$3.87^{+0.18}_{-0.38}$	$3.74^{+0.24}_{-0.24}$	–	8.71 ± 0.56	7.94 ± 0.49	–
0.600	$44.32^{+0.05}_{-0.05}$	$43.74^{+0.08}_{-0.07}$	–	$3.60^{+0.47}_{-0.75}$	$4.08^{+0.23}_{-0.25}$	–	8.16 ± 1.22	8.30 ± 0.47	–
0.602	$44.39^{+0.02}_{-0.02}$	$44.45^{+0.02}_{-0.02}$	–	$3.91^{+0.13}_{-0.16}$	$4.03^{+0.11}_{-0.13}$	–	8.81 ± 0.29	8.62 ± 0.24	–
0.647	$44.78^{+0.02}_{-0.02}$	$44.89^{+0.02}_{-0.02}$	–	$3.80^{+0.18}_{-0.28}$	$3.83^{+0.26}_{-0.52}$	–	8.67 ± 0.46	8.47 ± 0.78	–
0.676	$45.21^{+0.02}_{-0.02}$	$45.48^{+0.02}_{-0.02}$	–	$3.72^{+0.10}_{-0.17}$	$3.86^{+0.24}_{-0.66}$	–	8.62 ± 0.28	8.89 ± 0.90	–
0.676	$44.47^{+0.04}_{-0.04}$	$44.45^{+0.05}_{-0.05}$	–	$3.65^{+0.38}_{-0.73}$	$3.85^{+0.47}_{-0.82}$	–	8.31 ± 1.11	8.26 ± 1.29	–
0.719	$44.51^{+0.04}_{-0.04}$	$44.61^{+0.03}_{-0.03}$	–	$3.83^{+0.26}_{-0.84}$	$3.59^{+0.61}_{-0.58}$	–	8.66 ± 1.10	7.84 ± 1.18	–
0.808	$44.46^{+0.04}_{-0.04}$	$44.36^{+0.03}_{-0.03}$	–	$3.48^{+0.50}_{-0.68}$	$4.09^{+0.21}_{-0.49}$	–	7.96 ± 1.18	8.67 ± 0.70	–
0.825	$44.38^{+0.05}_{-0.05}$	$44.38^{+0.04}_{-0.04}$	–	$3.55^{+0.42}_{-0.39}$	$3.54^{+0.24}_{-0.18}$	–	8.07 ± 0.81	7.60 ± 0.42	–
0.884	–	$44.52^{+0.02}_{-0.02}$	–	–	$3.87^{+0.14}_{-0.23}$	–	–	8.34 ± 0.37	–
0.897	–	$44.68^{+0.03}_{-0.03}$	–	–	$4.09^{+0.16}_{-0.25}$	–	–	8.88 ± 0.41	–
0.986	–	$44.49^{+0.04}_{-0.04}$	–	–	$4.05^{+0.14}_{-0.18}$	–	–	8.67 ± 0.32	–
0.986	–	$44.75^{+0.02}_{-0.02}$	–	–	$3.71^{+0.19}_{-0.28}$	–	–	8.16 ± 0.46	–
1.002	–	$44.71^{+0.03}_{-0.03}$	–	–	$3.89^{+0.33}_{-0.51}$	–	–	8.50 ± 0.84	–
1.086	–	$44.65^{+0.03}_{-0.02}$	–	–	$3.99^{+0.17}_{-0.28}$	–	–	8.66 ± 0.45	–
1.194	–	$45.29^{+0.02}_{-0.01}$	–	–	$4.01^{+0.09}_{-0.10}$	–	–	9.08 ± 0.19	–
1.213	–	$45.64^{+0.01}_{-0.01}$	–	–	$3.94^{+0.13}_{-0.21}$	–	–	9.14 ± 0.35	–
1.223	–	$44.73^{+0.05}_{-0.04}$	–	–	$4.13^{+0.12}_{-0.13}$	–	–	8.98 ± 0.25	–
1.269	–	$45.20^{+0.02}_{-0.02}$	–	–	$3.76^{+0.24}_{-0.46}$	–	–	8.52 ± 0.70	–
1.286	–	$46.03^{+0.01}_{-0.01}$	–	–	$4.04^{+0.05}_{-0.06}$	–	–	9.57 ± 0.11	–
1.391	–	$45.31^{+0.02}_{-0.03}$	–	–	$3.78^{+0.22}_{-0.31}$	–	–	8.62 ± 0.53	–
1.394	–	$45.61^{+0.02}_{-0.02}$	–	–	$3.49^{+0.31}_{-0.39}$	–	–	8.22 ± 0.70	–
1.492	–	$45.44^{+0.03}_{-0.03}$	–	–	$4.09^{+0.12}_{-0.16}$	–	–	9.33 ± 0.29	–
1.514	–	$45.86^{+0.02}_{-0.02}$	–	–	$3.99^{+0.11}_{-0.13}$	–	–	9.37 ± 0.24	–
1.515	–	$45.07^{+0.05}_{-0.04}$	–	–	$4.05^{+0.15}_{-0.15}$	–	–	9.01 ± 0.29	–
1.584	–	$45.65^{+0.03}_{-0.03}$	$45.96^{+0.02}_{-0.02}$	–	$4.04^{+0.09}_{-0.09}$	$3.57^{+0.27}_{-0.27}$	–	9.33 ± 0.19	8.55 ± 0.54
1.605	–	$45.43^{+0.03}_{-0.03}$	$45.62^{+0.03}_{-0.03}$	–	$3.83^{+0.18}_{-0.22}$	$3.64^{+0.19}_{-0.20}$	–	8.80 ± 0.41	8.60 ± 0.39
1.647	–	$45.54^{+0.03}_{-0.03}$	$45.86^{+0.03}_{-0.03}$	–	$4.00^{+0.11}_{-0.11}$	$3.70^{+0.28}_{-0.33}$	–	9.20 ± 0.22	8.79 ± 0.61
1.674	–	$45.05^{+0.12}_{-0.12}$	$45.23^{+0.10}_{-0.10}$	–	$4.06^{+0.15}_{-0.40}$	$3.97^{+0.27}_{-0.42}$	–	9.03 ± 0.55	9.16 ± 0.69
1.685	–	$45.41^{+0.04}_{-0.04}$	$45.51^{+0.03}_{-0.03}$	–	$3.89^{+0.12}_{-0.16}$	$4.18^{+0.05}_{-0.06}$	–	8.91 ± 0.28	9.64 ± 0.11
1.728	–	$45.15^{+0.08}_{-0.08}$	$45.49^{+0.05}_{-0.05}$	–	$3.92^{+0.25}_{-0.37}$	$3.63^{+0.34}_{-0.35}$	–	8.80 ± 0.62	8.56 ± 0.69
1.743	–	$45.58^{+0.03}_{-0.03}$	$45.79^{+0.03}_{-0.03}$	–	$4.10^{+0.11}_{-0.15}$	$3.82^{+0.22}_{-0.37}$	–	9.43 ± 0.26	9.00 ± 0.59
1.862	–	$45.60^{+0.05}_{-0.05}$	$45.39^{+0.05}_{-0.05}$	–	$3.72^{+0.41}_{-0.80}$	$4.17^{+0.24}_{-0.71}$	–	8.68 ± 1.21	9.60 ± 0.95
1.902	–	$45.41^{+0.05}_{-0.05}$	$45.65^{+0.02}_{-0.02}$	–	$3.51^{+0.45}_{-0.39}$	$3.79^{+0.09}_{-0.08}$	–	8.15 ± 0.84	8.90 ± 0.16
1.902	–	$45.74^{+0.03}_{-0.03}$	$45.84^{+0.02}_{-0.02}$	–	$3.84^{+0.22}_{-0.57}$	$3.64^{+0.22}_{-0.29}$	–	9.00 ± 0.78	8.65 ± 0.51
1.960	–	$45.58^{+0.03}_{-0.03}$	$45.73^{+0.02}_{-0.02}$	–	$3.78^{+0.24}_{-0.53}$	$4.05^{+0.06}_{-0.07}$	–	8.78 ± 0.77	9.45 ± 0.13
1.963	–	$45.38^{+0.04}_{-0.04}$	$45.62^{+0.02}_{-0.02}$	–	$3.98^{+0.13}_{-0.16}$	$3.73^{+0.19}_{-0.24}$	–	9.07 ± 0.29	8.78 ± 0.43
2.003	–	$45.52^{+0.04}_{-0.04}$	$45.63^{+0.03}_{-0.03}$	–	$3.94^{+0.11}_{-0.13}$	$3.95^{+0.14}_{-0.25}$	–	9.06 ± 0.24	9.23 ± 0.39
2.031	–	$45.66^{+0.02}_{-0.03}$	$45.60^{+0.02}_{-0.02}$	–	$4.11^{+0.08}_{-0.12}$	$4.01^{+0.07}_{-0.06}$	–	9.49 ± 0.20	9.34 ± 0.13
2.033	–	$45.45^{+0.04}_{-0.04}$	$45.70^{+0.04}_{-0.03}$	–	$4.07^{+0.09}_{-0.10}$	$3.75^{+0.16}_{-0.18}$	–	9.28 ± 0.19	8.83 ± 0.34
2.041	–	$45.54^{+0.03}_{-0.03}$	$45.70^{+0.03}_{-0.03}$	–	$3.86^{+0.24}_{-0.32}$	$3.59^{+0.48}_{-0.52}$	–	8.93 ± 0.56	8.52 ± 1.00
2.305	–	–	$45.81^{+0.05}_{-0.05}$	–	–	$3.95^{+0.11}_{-0.12}$	–	–	9.26 ± 0.23
2.306	–	–	$46.17^{+0.02}_{-0.02}$	–	–	$4.07^{+0.08}_{-0.09}$	–	–	9.61 ± 0.17
2.351	–	–	$45.58^{+0.07}_{-0.07}$	–	–	$4.08^{+0.16}_{-0.22}$	–	–	9.48 ± 0.37
2.463	–	–	$46.63^{+0.02}_{-0.02}$	–	–	$3.95^{+0.07}_{-0.08}$	–	–	9.49 ± 0.15
2.581	–	–	$46.10^{+0.02}_{-0.02}$	–	–	$3.85^{+0.12}_{-0.29}$	–	–	9.15 ± 0.41
2.591	–	–	$46.02^{+0.02}_{-0.02}$	–	–	$4.11^{+0.06}_{-0.07}$	–	–	9.64 ± 0.14
2.594	–	–	$45.99^{+0.02}_{-0.02}$	–	–	$3.96^{+0.09}_{-0.11}$	–	–	9.34 ± 0.20

Notes. An extended version of this table containing SEP and SES measurements for all sources in the validation catalogue can be found here.
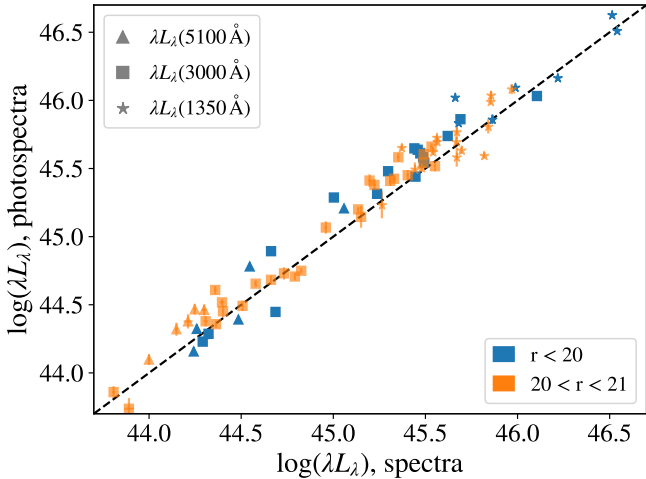
Fig. 5. Continuum luminosity measurements from SDSS spectra and miniJPAS photospectra. Triangles, squares, and stars indicate the continuum luminosity at $\lambda = 5100$, 3000, and 1350 Å, respectively. Blue and orange symbols display the results for sources with $r < 20$ and $20 < r < 21$, error bars denote 1σ-equivalent uncertainties, and the dashed line indicates a 1:1 relation between SES and SEP measurements.

4.1. Continuum luminosity

In Fig. 5, we display continuum luminosity measurements from SDSS spectra and miniJPAS photospectra for the 54 quasars in the validation sample. Triangles, squares, and stars indicate the continuum luminosity at $\lambda = 5100$, 3000, and 1350 Å, respectively, and blue and orange symbols display the results for sources with $r < 20$ and $20 < r < 21$, and the dashed line indicates a 1:1 relation between SES and SEP measurements. Error bars denote 1σ-equivalent uncertainties from spectral and photometric decomposition. As we can see, these uncertainties do not capture the dispersion of measurements between SDSS spectra and miniJPAS photospectra; this is likely because error bars do not attempt to capture the impact of variability on the results, which is an important source on uncertainty in the comparison between spectroscopic and photometric measurements (see Sect. 2.3).

We find a small systematic difference between photometric and spectroscopic measurements: the mean and standard deviation of their difference are -0.11 and 0.11 dex for $\lambda L_\lambda (5100\,\text{Å})$, -0.07 and 0.11 dex for $\lambda L_\lambda (3000\,\text{Å})$, and -0.07 and 0.12 dex for $\lambda L_\lambda (1350\,\text{Å})$. We check that this bias is sensitive to the photometric correction used to convert aperture to total magnitudes (see Sect. 2.3), and that it disappears by slightly decreasing such a correction. Nonetheless, it is crucial to keep in mind that a constant bias has negligible impact on the computation of SMBH masses because the recalibration of virial coefficients absorbs it (see Sect. 3.4).

4.2. Emission line properties

In Fig. 6, we display EW (top row) and FWHM (bottom row) measurements from SDSS spectra and miniJPAS photospectra for the 54 quasars in the validation sample. The left, middle, and right panels show the results for Hβ, Mg II, and C IV, respectively. These lines are broader than $1500\,\text{km\,s}^{-1}$ for all sources, and thus we expect accurate FWHM measurements from miniJPAS photospectra (see Sect. 3.5). The symbol ρ indicates the Pearson correlation coefficient between spectro-

scopic and photometric measurements. As we can see, EWs and FWHMs present much larger error bars than continuum luminosity measurements, reflecting the complexity of extracting line properties. The median precision of EW and FWHM measurements from photometric data is 16 and 30%, respectively, and from spectroscopic data is 6 and 8%. Therefore, at fixed r-band apparent magnitude, spectroscopic measurements from SDSS are between two to four times more precise than photometric measurements from miniJPAS. We note that these error bars do not attempt to capture the impact of variability on the comparison between spectroscopic and photometric measurements (see Sect. 2.3).

We find that the Person correlation coefficient between spectroscopic and photometric FWHM measurements is almost unity for Hβ, close to $\rho = 0.5$ for C IV, and approximately $\rho = 0.3$ for Mg II. The modest value of the correlation coefficient for some lines is likely caused by the combination of the limited S/N of observations quasar variability. Nonetheless, the agreement between emission line properties from spectroscopic and photometric measurements is substantial: we find that the mean and standard deviation of the difference for EWs are 0.15 and 0.36 dex for Hβ, -0.07 and 0.19 dex for Mg II, and 0.09 and 0.17 dex for C IV, and for FWHM -0.06 and 0.09 dex for Hβ, -0.28 and 0.19 dex for Mg II, and -0.20 and 0.18 dex for C IV. We thus find a systematic difference between FWHM measurements from SDSS spectra and miniJPAS photospectra, possibly because we use a single component to fit line profiles while Rakshit et al. (2020) does so using multiple components (see Sect. 3.3). We note that differences of the same order are found between widths measured by spectral decomposition methods using a single and multiple components (e.g. Shen et al. 2011; Rakshit et al. 2020). However, it is essential to notice that a constant bias has a negligible impact on the computation of SMBH masses because the recalibration of virial coefficients absorbs it (see Sect. 3.4).

4.3. SMBH virial masses

Before computing SMBH virial masses, we recalibrated the virial coefficients of Eq. (2) to correct for possible systematic differences between SES and SEP measurements due to the different methodologies to compute continuum luminosities and emission line properties. Following the approach explained in Sect. 3.4, we find $A = 0.876 \pm 0.005$ and $B = 0.263 \pm 0.013$ for Hβ, $A = 0.292 \pm 0.017$ and $B = 0.590 \pm 0.006$ for Mg II, and $A = 0.894 \pm 0.125$ and $B = 0.263 \pm 0.029$ for C IV.

In Fig. 7, we compare different SMBH mass estimates for quasars in the validation sample: SEP masses from miniJPAS photospectra produced using the previous coefficients and SES masses from SDSS spectra generated using the coefficients quoted in Sect. 3.4. The middle and bottom sub-panels show the mean and standard deviation of the logarithmic difference between spectroscopic and photometric measurements, respectively. Horizontal error bars denote 1σ uncertainties for SES masses, which are computed via error propagation of Eq. (2) (see Rakshit et al. 2020). We compute error bars for SEP masses following the previous approach for a fair comparison between spectroscopic and photometric error estimates. As we can see, the size of error bars decreases with the mass of the sources for both techniques, reflecting the increasingly larger precision of measurements for brighter sources, and at fixed apparent magnitude, for sources with broader lines (see Sect. 3.4). We note that error bars do not capture the impact of systematic uncertainties affecting single-epoch masses.
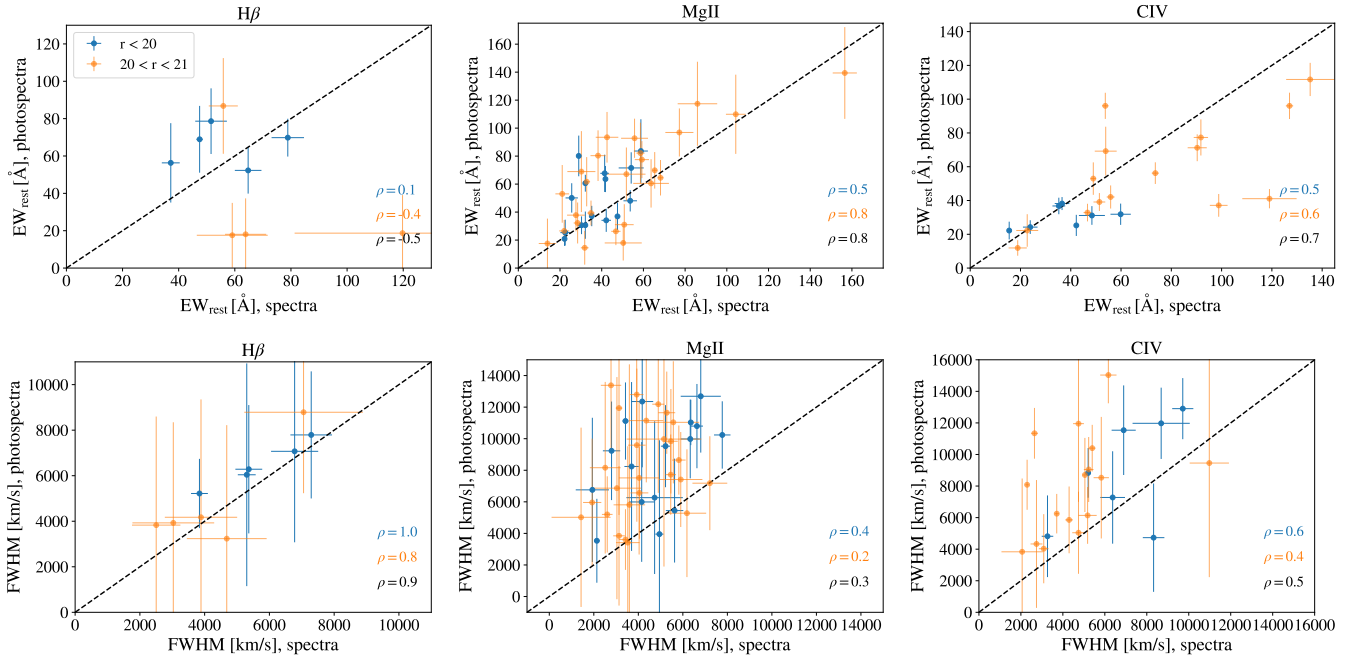
Fig. 6. EW (*top row*) and FWHM (*bottom row*) measurements from SDSS spectra and miniJPAS photospectra. *Left, middle*, and *right panels*: results for Hβ, Mg II, and C IV, respectively. Dashed lines indicate a 1:1 relation between photometric and spectroscopic measurements. The symbol ρ indicates the Pearson correlation coefficient between spectroscopic and photometric measurements.
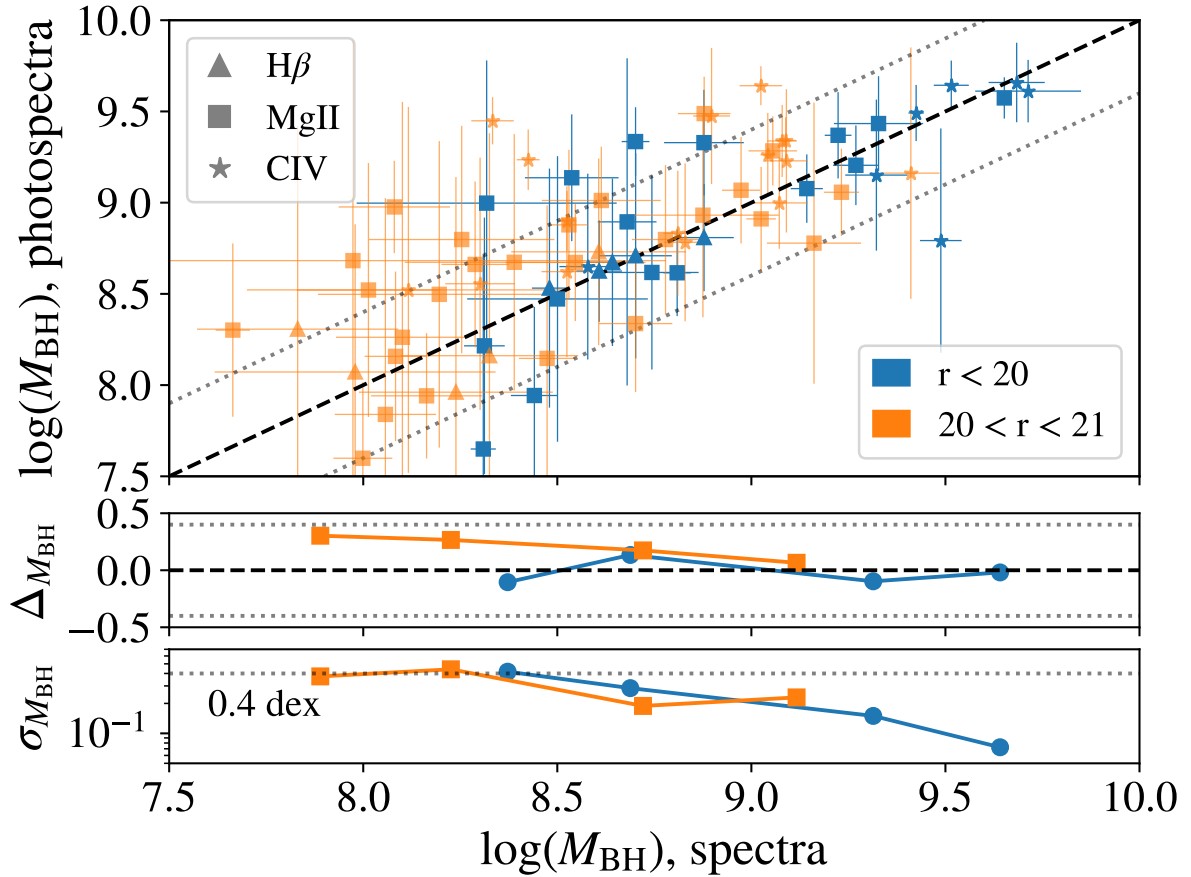
Fig. 7. SMBH mass measurements from SDSS spectra and miniJPAS photospectra. The *middle* and *bottom sub-panels* display the mean and standard deviation of the logarithmic difference between spectroscopic and photometric measurements, respectively, the dashed line indicates a 1:1 relation between these measurements, and dotted lines are displaced 0.4 dex from such a relation. As we can see, there is a remarkable agreement between SES and SEP masses, with most measurements less than 1σ away from the 1:1 relation.

We find that SEP and SES masses display a remarkable agreement, with no systematic difference between these and most measurements less than 1σ away from the 1:1 relation. We can thus conclude that SEP delivers unbiased measurements of SMBH masses despite the limited spectral resolution of J-PAS photospectra. We also find that the standard deviation of the difference between spectroscopic and photometric measurements decreases with the mass of the sources: it ranges from 0.4 to 0.07 dex for SMBHs with masses from $\log(M_{\rm BH}/M_\odot) \simeq 8$ to 9.75, respectively. This level of precision is in line with our forecasts from simulated miniJPAS observations (see Sect. 3.5), suggesting limited impact unresolved emission lines, host-galaxy contamination, and other effects on continuum luminosity and emission line properties (see Sects. 3.2 and 3.3).

It is a well-established observational result that black hole mass estimates show a residual dependence on the Eddington ratio (Du et al. 2016, 2018; Grier et al. 2017; Du & Wang 2019; Martínez-Aldama et al. 2019; Fonseca Alvarez et al. 2020; Dalla Bontà et al. 2020), which serves as a measure of the accretion rate of the system. Therefore, it is conceivable that the performance of SEP could depend upon the Eddington ratio,

$$R_{\rm Edd} = L_{\rm bol}/L_{\rm Edd}, \qquad (3)$$

where $L_{\rm Edd} = 1.257 \times 10^{38}(M_{\rm BH}/M_\odot)$ is the Eddington luminosity, while $L_{\rm bol}$ is the bolometric luminosity, which we estimate from the monochromatic luminosity at 5100, 3000, and 1350 Å using $L_{\rm bol} = 9.26\,L_{5100}$, $5.15\,L_{3000}$, and $3.81\,L_{1350}$, respectively (Shen et al. 2011). We note that the previous expressions can result in uncertainties as large as a factor of two (Richards et al. 2006); this is because precise estimation of bolometric luminosities requires observations of the spectral energy distribution from X-ray to radio.

In Fig. 8, we display Eddington ratio measurements from miniJPAS photospectra as a function of SEP masses. The colour of the symbols indicates the logarithmic difference between mass measurements from SDSS spectra and miniJPAS photospectra. As we can see, there is no apparent dependence of the mass difference upon the Eddington ratio, letting us conclude that the performance of SEP is independent of the Eddington luminosity of the system.

Another important consideration is that SEP faces similar systematic uncertainties as SES, including the chosen measurement that characterises line widths, different assumptions involving spectral decomposition methods, host-galaxy contamination, broad absorption lines, outflows, residual dependence of SMBH masses on the Eddington ratio, uncertainties in the relation between continuum luminosity and BLR size, variations in the virial factor with the BLR geometry, and possible non-reverberating components of some emission lines (for a recent detailed discussion about these effects see Dalla Bontà et al. 2020). The aforementioned effects induce differences of the order of 0.4 dex between RM and SES masses, with little dependence on SMBH mass (e.g. Grier et al. 2019; Homayouni et al. 2020; Dalla Bontà et al. 2020). If we assume that the impact of the previous systematics on SES and SEP is of the same order, we can compare the precision of these techniques measuring SMBH masses. For SMBHs with masses of the order of $\log(M_{\rm BH}/M_\odot) = 8$, the standard deviation of the difference between SES and SEP masses is of the same order as the impact of systematic uncertainties, suggesting that SEP masses are $\sqrt{2} \simeq 1.4$ times less precise than SES masses. Systematic uncertainties progressively dominate the error budget for SMBH with larger masses; for sources with $\log(M_{\rm BH}/M_\odot) \simeq 9.0$
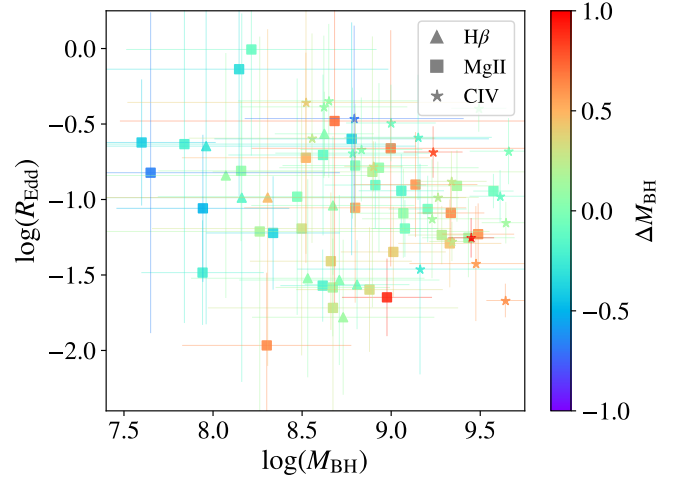
Fig. 8. Performance of SEP as a function of Eddington ratio. Symbols indicate results from miniJPAS photospectra, and their colour denotes the logarithmic difference between mass measurements from SDSS spectra and miniJPAS photospectra. As we can see, the mass difference shows no dependence upon the Eddington ratio.

and 9.5, SES masses are only 12 and 3% more precise than SEP masses, respectively. We can thus conclude that SEP yields SMBH virial masses with only mildly lower precision than SES for the majority of sources in the validation sample. However, a more thorough study of the accuracy of SEP requires sources with both RM and SEP masses.

5. Conclusions

Precise measurements of SMBH masses are crucial for characterising the properties of the SMBH population, understanding the links between SMBHs and their host galaxies, and using quasars as large-scale structure tracers for multiple cosmological applications. In this work, we develop a novel approach for measuring SMBH virial masses from single-epoch, narrow-band photometric observations. We summarise our main findings as follows:

- In Sect. 3 we describe a Bayesian-based approach for measuring continuum luminosities and emission line properties from narrow-band photometric data. We validate our methodology using simulated J-PAS observations, finding that they can deliver accurate continuum luminosities for sources brighter than $r = 21$ and unbiased FWHM measurements for lines broader than $\simeq 1500\,{\rm km\,s^{-1}}$. For the kinds of quasars we consider here, this value translates into a minimum SMBH mass of approximately $\log(M_{\rm BH}/M_\odot) = 8$.
- In Sect. 4 we characterise the performance of our methodology using 54 SDSS quasars observed by the miniJPAS survey, a proof-of-concept project of the J-PAS Collaboration covering $\approx 1\,{\rm deg^2}$ of the northern sky using the 56 J-PAS narrow-band filters. We find that the standard deviation of the difference between SES measurements from SDSS and SEP measurements from miniJPAS is approximately 0.1 and 0.2 dex for continuum luminosities and FWHMs, respectively. However, we caution that quasar variability is a significant source of uncertainty for this comparison.
- In Fig. 7 we compare SES masses from SDSS and SEP masses from miniJPAS, finding that both are compatible within error bars. We also show that the standard deviation of the difference between spectroscopic and photometric

measurements ranges from 0.4 to 0.07 dex for masses from $\log(M_{BH}/M_\odot) \simeq 8$ to 9.75, respectively. Reverberation mapping studies show that SES masses are affected by systematic uncertainties of the order of 0.4 dex; given that SES and SEP face similar systematics, we can conclude that SEP yields SMBH virial masses with only mildly lower precision than SES for the majority of sources in the validation sample.

Throughout this work, we have focused on characterising the precision SEP for the J-PAS survey, which will soon start observing thousands of square degrees of the northern sky without applying any source preselection other than the photometric depth in the detection band. Therefore, SEP has the potential to provide details on the physical properties of new types of quasar populations that do not satisfy the preselection criteria of previous spectroscopic surveys. We have shown that our current technique delivers precise measurements only for sources brighter than $r = 21$; to push our technique towards fainter magnitudes, we plan to measure SMBH virial masses from stacked photospectra of low signal-to-noise sources. Taken together, we expect J-PAS and SEP to be of paramount importance for completing our knowledge of SMBH demographics across cosmic time.

To estimate the performance of our methodology, we have relied upon SDSS sources with both SES and SEP measurements. Due to the limited precision of SES measurements, we would have rather used quasars with SEP and either RM or direct mass measurements; however, we did not find any source with these more precise mass measurements within the miniJ-PAS footprint. On the other hand, the J-PAS survey will soon observe quasars with these types of mass measurements, thereby enabling a better characterisation of the performance of SEP. Furthermore, we will have more sources available for statistical studies, which will enable a more precise assessment of the performance of our novel technique for sources with different Eddington ratios and redshifts.

Although our technique was developed to analyse J-PAS photospectra, SEP can also be used to compute SMBH masses for quasars observed by other surveys without substantial modifications. For instance, we could use this methodology to analyse data from multi-band surveys with enough spectral resolution to resolve the profile of broad emission lines, such as SHARDS and PAUS, and low-resolution spectroscopic surveys covering an extensive wavelength range, such as *Gaia* (Gaia Collaboration 2012) and the Spectro-Photometer for the History of the Universe, Epoch of Reionization and Ices Explorer (SPHEREx) survey (Doré et al. 2014).

References

Abramo, L. R., Strauss, M. A., Lima, M., et al. 2012, MNRAS, 423, 3251
Abramowicz, M. A., & Fragile, P. C. 2013, Liv. Rev. Rel., 16, 1
Aird, J., Nandra, K., Laird, E. S., et al. 2010, MNRAS, 401, 2531
Alarcon, A., Gaztanaga, E., Eriksen, M., et al. 2021, MNRAS, 501, 6103
Astropy Collaboration (Robitaille, T. P., et al.) 2013, A&A, 558, A33
Astropy Collaboration (Price-Whelan, A. M., et al.) 2018, AJ, 156, 123
Baldwin, J. A. 1977, ApJ, 214, 679
Bañados, E., Venemans, B. P., Mazzucchelli, C., et al. 2018, Nature, 553, 473
Benitez, N., Dupke, R., Moles, M., et al. 2014, ArXiv e-prints [arxiv:1403.5237]
Benítez, N., Gaztañaga, E., Miquel, R., et al. 2009, ApJ, 691, 241
Bentz, M. C., Peterson, B. M., Pogge, R. W., Vestergaard, M., & Onken, C. A. 2006, ApJ, 644, 133
Bentz, M. C., Peterson, B. M., Netzer, H., Pogge, R. W., & Vestergaard, M. 2009, ApJ, 697, 160
Bentz, M. C., Denney, K. D., Grier, C. J., et al. 2013, ApJ, 767, 149
Blandford, R. D., & McKee, C. F. 1982, ApJ, 255, 419
Bonoli, S., Calderone, G., Abramo, R., et al. 2021, in Nuclear Activity in Galaxies Across Cosmic Time, eds. M. Pović, P. Marziani, J. Masegosa, et al., IAU Symp., 356, 12
Bonoli, S., Marín-Franch, A., Varela, J., et al. 2021, A&A, 653, A31
Brauneck, U., Sprengard, R., Bourquin, S., & Marín-Franch, A. 2018a, J. Astron. Telesc. Instrum. Syst., 4, 015002
Brauneck, U., Sprengard, R., Bourquin, S., & Marín-Franch, A. 2018b, J. Astron. Telesc. Instrum. Syst., 4, 015003
Broyden, C. G. 1970, IMA J. Appl. Math., 6, 76
Busca, N. G., Delubac, T., Rich, J., et al. 2013, A&A, 552, A96
Calderone, G., Nicastro, L., Ghisellini, G., et al. 2017, MNRAS, 472, 4051
Caplar, N., Lilly, S. J., & Trakhtenbrot, B. 2017, ApJ, 834, 111
Castorina, E., Hand, N., Seljak, U., et al. 2019, JCAP, 2019, 010
Chambers, K. C., Magnier, E. A., Metcalfe, N., et al. 2016, ArXiv e-prints [arXiv:1612.05560]
Chaves-Montero, J., Bonoli, S., Salvato, M., et al. 2017, MNRAS, 472, 2085
Collin, S., Kawaguchi, T., Peterson, B. M., & Vestergaard, M. 2006, A&A, 456, 75
Cristiani, S., & Vio, R. 1990, A&A, 227, 385
Croton, D. J., Springel, V., White, S. D. M., et al. 2006, MNRAS, 365, 11
Czerny, B., & Hryniewicz, K. 2011, A&A, 525, L8
Dalcin, L., & Fang, Y.-L. L. 2021, Comput. Sci. Eng., 23, 47
Dalcín, L., Paz, R., & Storti, M. 2005, J. Parallel Distrib. Comput., 65, 1108
Dalcín, L., Paz, R., Storti, M., & D'Elía, J. 2008, J. Parallel Distrib. Comput., 68, 655
Dalcin, L. D., Paz, R. R., Kler, P. A., & Cosimo, A. 2011, Adv. Water Resour., 34, 1124
Dalla Bontà, E., Peterson, B. M., Bentz, M. C., et al. 2020, ApJ, 903, 112
Davidson, K., & Netzer, H. 1979, Rev. Mod. Phys., 51, 715
Davies, R. I., Tacconi, L. J., & Genzel, R. 2004a, ApJ, 613, 781
Davies, R. I., Tacconi, L. J., & Genzel, R. 2004b, ApJ, 602, 148
Davies, R. I., Thomas, J., Genzel, R., et al. 2006, ApJ, 646, 754
Davies, F. B., Hennawi, J. F., Bañados, E., et al. 2018, ApJ, 864, 142

Davis, M., Guhathakurta, P., Konidaris, N. P., et al. 2007, ApJ, 660, L1
Dawson, K. S., Schlegel, D. J., Ahn, C. P., et al. 2013, AJ, 145, 10
Dawson, K. S., Kneib, J.-P., Percival, W. J., et al. 2016, AJ, 151, 44
Delvecchio, I., Gruppioni, C., Pozzi, F., et al. 2014, MNRAS, 439, 2736
Denney, K. D., Horne, K., Shen, Y., et al. 2016, ApJS, 224, 14
Di Matteo, T., Springel, V., & Hernquist, L. 2005, Nature, 433, 604
Dong, X.-B., Wang, T.-G., Wang, J.-G., et al. 2009, ApJ, 703, L1
Doré, O., Bock, J., Ashby, M., et al. 2014, ArXiv e-prints [arxiv:1412.4872]
Du, P., & Wang, J.-M. 2019, ApJ, 886, 42
Du, P., Lu, K.-X., Zhang, Z.-X., et al. 2016, ApJ, 825, 126
Du, P., Zhang, Z.-X., Wang, K., et al. 2018, ApJ, 856, 6
Dubois, Y., Devriendt, J., Slyz, A., & Teyssier, R. 2012, MNRAS, 420, 2662
Eisenstein, D. J., Weinberg, D. H., Agol, E., et al. 2011, AJ, 142, 72
Eriksen, M., Alarcon, A., Gaztanaga, E., et al. 2019, MNRAS, 484, 4200
Fan, X., Strauss, M. A., Becker, R. H., et al. 2006, AJ, 132, 117
Ferrarese, L., & Merritt, D. 2000, ApJ, 539, L9
Fletcher, R. 1970, Comput. J., 13, 317
Fonseca Alvarez, G., Trump, J. R., Homayouni, Y., et al. 2020, ApJ, 899, 73
Foreman-Mackey, D., Hogg, D. W., Lang, D., & Goodman, J. 2013, PASP, 125, 306
Gaia Collaboration (Prusti, T., et al.) 2012, MNRAS, 423, 3251
Gebhardt, K., Bender, R., Bower, G., et al. 2000, ApJ, 539, L13
Goldfarb, D. 1970, Math. Comput., 24, 23
González Delgado, R. M., Díaz-García, L. A., de Amorim, A., et al. 2021, A&A, 649, A79
Grandi, S. A. 1982, ApJ, 255, 25
Greene, J. E., & Ho, L. C. 2005, ApJ, 630, 122
Grier, C. J., Trump, J. R., Shen, Y., et al. 2017, ApJ, 851, 21
Grier, C. J., Shen, Y., Horne, K., et al. 2019, ApJ, 887, 38
Gültekin, K., Richstone, D. O., Gebhardt, K., et al. 2009, ApJ, 698, 198
Guo, H., Shen, Y., & Wang, S. 2018, Astrophysics Source Code Library [record ascl:1809.008]
Guo, H., Liu, X., Shen, Y., et al. 2019, MNRAS, 482, 3288
Harris, C. R., Millman, K. J., van der Walt, S. J., et al. 2020, Nature, 585, 357
Hernán-Caballero, A., Hatziminaoglou, E., Alonso-Herrero, A., & Mateos, S. 2016, MNRAS, 463, 2064
Hernán-Caballero, A., Varela, J., López-Sanjuan, C., et al. 2021, A&A, 654, A101
Hicks, E. K. S., & Malkan, M. A. 2008, ApJS, 174, 31
Ho, L. 1999, Observational Evidence for the Black Holes in the Universe, 234, 157
Homayouni, Y., Trump, J. R., Grier, C. J., et al. 2020, ApJ, 901, 55
Hook, I. M., McMahon, R. G., Boyle, B. J., & Irwin, M. J. 1994, MNRAS, 268, 305
Hopkins, P. F., Strauss, M. A., Hall, P. B., et al. 2004, AJ, 128, 1112
Hou, J., Sánchez, A. G., Ross, A. J., et al. 2021, MNRAS, 500, 1201
Hoyle, F., & Fowler, W. A. 1963, MNRAS, 125, 169
Hunter, J. D. 2007, Comput. Sci. Eng., 9, 90
Inayoshi, K., Visbal, E., & Haiman, Z. 2020, ARA&A, 58, 27
Jensen, T. W., Vivek, M., Dawson, K. S., et al. 2016, ApJ, 833, 199
Kaspi, S., Smith, P. S., Netzer, H., et al. 2000, ApJ, 533, 631
Kaspi, S., Maoz, D., Netzer, H., et al. 2005, ApJ, 629, 61
Kaspi, S., Brandt, W. N., Maoz, D., et al. 2021, ApJ, submitted [arXiv:2106.00691]
Kelly, B. C., Bechtold, J., & Siemiginowska, A. 2009, ApJ, 698, 895
King, A. 2003, ApJ, 596, L27
Kollatschny, W., & Zetzl, M. 2013, A&A, 549, A100
Kormendy, J., & Ho, L. C. 2013, ARA&A, 51, 511
Kormendy, J., & Richstone, D. 1995, ARA&A, 33, 581
Kozłowski, S., Kochanek, C. S., Ashby, M. L. N., et al. 2016, ApJ, 817, 119
Lira, P., Kaspi, S., Netzer, H., et al. 2018, ApJ, 865, 56
Lumbreras-Calle, A., Muñoz-Tuñón, C., Méndez-Abreu, J., et al. 2019, A&A, 621, A52
Lynden-Bell, D. 1969, Nature, 223, 690
MacLeod, C. L., Ivezić, Ž., Kochanek, C. S., et al. 2010, ApJ, 721, 1014
MacLeod, C. L., Ivezić, Ž., Sesar, B., et al. 2012, ApJ, 753, 106
Magorrian, J., Tremaine, S., Richstone, D., et al. 1998, AJ, 115, 2285
Marconi, A., & Hunt, L. K. 2003, ApJ, 589, L21
Marinello, M., Overzier, R. A., Röttgering, H. J. A., et al. 2020, MNRAS, 492, 1991
Martínez-Aldama, M. L., Czerny, B., Kawka, D., et al. 2019, ApJ, 883, 170
Martínez-Solaeche, G., González Delgado, R. M., García-Benito, R., et al. 2021, A&A, 647, A158
McConnell, N. J., & Ma, C.-P. 2013, ApJ, 764, 184
McKay, M. D., Beckman, R. J., & Conover, W. J. 1979, Technometrics, 21, 239
McLure, R. J., & Jarvis, M. J. 2002, MNRAS, 337, 109
Mejía-Restrepo, J. E., Lira, P., Netzer, H., Trakhtenbrot, B., & Capellupo, D. M. 2018, Nat. Astron., 2, 63

Merloni, A., Rudnick, G., & Di Matteo, T. 2004, MNRAS, 354, L37
Meusinger, H., & Weiss, V. 2013, A&A, 560, A104
Miralda-Escudé, J. 1998, ApJ, 501, 15
Moles, M., Benítez, N., Aguerri, J. A. L., et al. 2008, AJ, 136, 1325
Mortlock, D. J., Warren, S. J., Venemans, B. P., et al. 2011, Nature, 474, 616
Nagao, T., Marconi, A., & Maiolino, R. 2006, A&A, 447, 157
Netzer, H., & Peterson, B. M. 1997, Astron. Time Ser., 218, 85
Oke, J. B., & Gunn, J. E. 1983, ApJ, 266, 713
Oke, J. B., Shields, G. A., & Korycansky, D. G. 1984, ApJ, 277, 64
Onken, C. A., Valluri, M., Peterson, B. M., et al. 2007, ApJ, 670, 105
Palanque-Delabrouille, N., Magneville, C., Yèche, C., et al. 2013, A&A, 551, A29
Palanque-Delabrouille, N., Magneville, C., Yèche, C., et al. 2016, A&A, 587, A41
Pâris, I., Petitjean, P., Ross, N. P., et al. 2017, A&A, 597, A79
Pâris, I., Petitjean, P., Aubourg, E., et al. 2018, A&A, 613, A51
Perez, F., & Granger, B. E. 2007, Comput. Sci. Eng., 9, 21
Pérez-González, P. G., Cava, A., Barro, G., et al. 2013, ApJ, 762, 46
Peterson, B. M. 1993, PASP, 105, 247
Peterson, B. M. 2014, Space Sci. Rev., 183, 253
Pieri, M. M., Bonoli, S., Chaves-Montero, J., et al. 2016, in SF2A-2016: Proceedings of the Annual meeting of the French Society of Astronomy and Astrophysics, eds. C. Reylé, J. Richard, L. Cambrésy, et al., 259
Pillepich, A., Springel, V., Nelson, D., et al. 2018, MNRAS, 473, 4077
Planck Collaboration VI. 2014, A&A, 571, A16
Rakshit, S., Stalin, C. S., & Kotilainen, J. 2020, ApJS, 249, 17
Richards, G. T., Lacy, M., Storrie-Lombardi, L. J., et al. 2006, ApJS, 166, 470
Richards, G. T., Kruczek, N. E., Gallagher, S. C., et al. 2011, AJ, 141, 167
Rickard, S., & Daniel, S. 2018, pyDOE2: An Experimental Design Package for Python, https://github.com/clicumu/pyDOE2
Risaliti, G., & Lusso, E. 2019, Nat. Astron., 3, 272
Salpeter, E. E. 1964, ApJ, 140, 796
Schaye, J., Crain, R. A., Bower, R. G., et al. 2015, MNRAS, 446, 521
Shankar, F., Weinberg, D. H., & Miralda-Escudé, J. 2009, ApJ, 690, 20
Shanno, D. F., & Kettler, P. C. 1970, Math. Comput., 24, 657
Shen, Y. 2013, Bull. Astron. Soc. India, 41, 61
Shen, Y., Richards, G. T., Strauss, M. A., et al. 2011, ApJS, 194, 45
Shen, Y., Brandt, W. N., Richards, G. T., et al. 2016, ApJ, 831, 7
Shen, Y., Hall, P. B., Horne, K., et al. 2019, ApJS, 241, 34
Sijacki, D., Vogelsberger, M., Genel, S., et al. 2015, MNRAS, 452, 575
Silk, J., & Rees, M. J. 1998, A&A, 331, L1
Silverman, J. D., Green, P. J., Barkhouse, W. A., et al. 2008, ApJ, 679, 118
Sobral, D., Santos, S., Matthee, J., et al. 2018, MNRAS, 476, 4725
Somerville, R. S., Hopkins, P. F., Cox, T. J., Robertson, B. E., & Hernquist, L. 2008, MNRAS, 391, 481
Taniguchi, Y., Kajisawa, M., Kobayashi, M. A. R., et al. 2015, PASJ, 67, 104
Tokunaga, A. T., & Vacca, W. D. 2005, PASP, 117, 421
Trakhtenbrot, B., & Netzer, H. 2012, MNRAS, 427, 3081
Tremaine, S., Gebhardt, K., Bender, R., et al. 2002, ApJ, 574, 740
van Dokkum, P. G., Labbé, I., Marchesini, D., et al. 2009, PASP, 121, 2
Vanden Berk, D. E., Richards, G. T., Bauer, A., et al. 2001, AJ, 122, 549
Véron-Cetty, M.-P., Joly, M., & Véron, P. 2004, A&A, 417, 515
Vestergaard, M. 2002, ApJ, 571, 733
Vestergaard, M., & Peterson, B. M. 2006, ApJ, 641, 689
Virtanen, P., Gommers, R., Oliphant, T. E., et al. 2020, Nat. Meth., 17, 261
Wandel, A., Peterson, B. M., & Malkan, M. A. 1999, ApJ, 526, 579
Wang, J.-M., Du, P., Hu, C., et al. 2014, ApJ, 793, 108
Wang, F., Davies, F. B., Yang, J., et al. 2020, ApJ, 896, 23
Wang, F., Yang, J., Fan, X., et al. 2021, ApJ, 907, L1
Watson, D., Denney, K. D., Vestergaard, M., & Davis, T. M. 2011, ApJ, 740, L49
Weinberger, R., Springel, V., Hernquist, L., et al. 2017, MNRAS, 465, 3291
Williams, P. R., Pancoast, A., Treu, T., et al. 2018, ApJ, 866, 75
Wills, B. J., Netzer, H., & Wills, D. 1985, ApJ, 288, 94
Yang, G., Brandt, W. N., Vito, F., et al. 2018, MNRAS, 475, 1887
Yang, J., Wang, F., Fan, X., et al. 2020a, ApJ, 897, L14
Yang, J., Wang, F., Fan, X., et al. 2020b, ApJ, 904, 26
York, D. G., Adelman, J., Anderson, J. E., Jr, et al. 2000, AJ, 120, 1579

1 Donostia International Physics Center, Paseo Manuel de Lardizabal 4, 20018 Donostia-San Sebastian, Spain
e-mail: jonas.chaves@dipc.org
2 Ikerbasque, Basque Foundation for Science, 48013 Bilbao, Spain
3 School of Physics and Astronomy, Tel Aviv University, Tel Aviv 69978, Israel
4 Facultad de Ciencias Físicas, Universidad Complutense de Madrid, Plaza de Ciencias, 1, 28040 Madrid, Spain

[5] Departamento de Astronomia, Instituto de Física, Universidade Federal do Rio Grande do Sul (UFRGS), Av. Bento Gonçalves, 9500 Porto Alegre, RS, Brazil

[6] Instituto de Física, Universidade de São Paulo, Rua do Matão 1371, CEP 05508-090 São Paulo, Brazil

[7] Instituto de Astrofísica de Andalucía (CSIC), PO Box 3004, 18080 Granada, Spain

[8] Centro de Estudios de Física del Cosmos de Aragón (CEFCA), Plaza San Juan, 1, 44001 Teruel, Spain

[9] Instituto de Astrofísica de Canarias, Calle Vía Láctea s/n, 38205 La Laguna, Spain

[10] Departamento de Astrofísica, Universidad de La Laguna, 38205 La Laguna, Spain

[11] Centro de Estudios de Física del Cosmos de Aragón (CEFCA), Unidad Asociada al CSIC, Plaza San Juan, 1, 44001 Teruel, Spain

[12] Observatório Nacional/MCTIC, Rua General José Cristino, 77, São Cristóvão, Rio de Janeiro, RJ 20921-400, Brazil

[13] Institute of Astronomy, Geophysics and Atmospheric Sciences, University of São Paulo, Rua do Matão, 1226, São Paulo, SP 05508-090, Brazil

[14] Department of Physics, Lancaster University, Lancaster LA1 4YB, UK

[15] Instituto de Física, Universidade Federal da Bahia, 40210-340 Salvador, BA, Brazil

[16] Department of Astronomy, University of Michigan, 311 West Hall, 1085 South University Ave., Ann Arbor, USA

[17] University of Alabama, Department of Physics and Astronomy, Gallalee Hall, Tuscaloosa, AL 35401, USA

[18] Instruments4, 4121 Pembury Place, La Canada Flintridge, CA 91011, USA

Appendix A: Forward- versus backward-modelling observations

In this section we study if we can extract unbiased measurements of emission line widths by backward-modelling quasar observations.
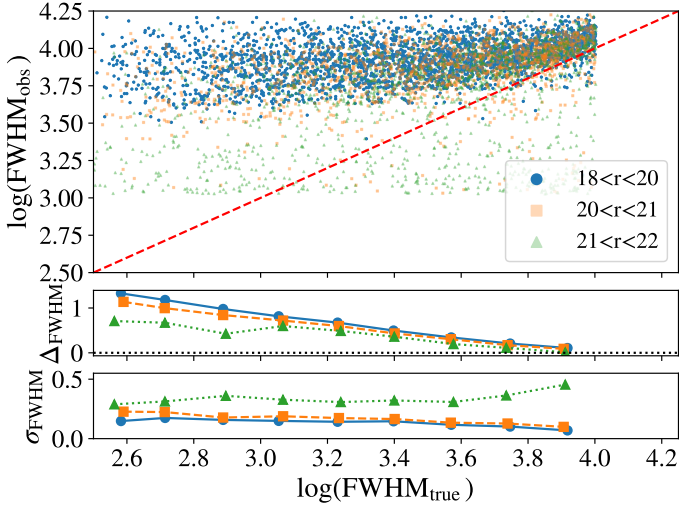

Fig. A.1. Backward-modelling measurements of C IV FWHMs from simulated J–PAS observations. This approach results in biased FWHM measurements even for lines as wide as $10\,000\,\mathrm{km\,s^{-1}}$, while forward-modelling observations enable FWHMs of lines broader than $1500\,\mathrm{km\,s^{-1}}$ in an unbiased fashion.

To backward-modelling emission line widths, we first estimate the quasar continuum emission following the same approach as in Sect. 3.2, and then we subtract it from observations to produce a line-only spectrum. After that, we identify the J–PAS bands in which the centre of the broad emission lines Hβ, Mg II, and C IV fall; if one of these lines falls between two J–PAS bands, we select the band with the maximum flux. Finally, we compute the FWHM of each line by subtracting the wavelengths at which the continuum emission intercepts half the flux of the band at which the centre of the line falls. We note that we perform a linear interpolation of the flux between J–PAS bands to improve the resolution of the results.

In Sect. 3.5, we use simulated J–PAS photospectra to study the impact of both the limited spectral resolution of J–PAS and photometric errors on SEP. In Fig. A.1, we show the result of backward-modelling the C IV width from simulated J–PAS observations. We can readily see that this approach results in biased FWHM measurements even for emission lines as broad as $10\,000\,\mathrm{km\,s^{-1}}$. In Fig. 3, we show that forward-modelling observations enables the FWHM of lines as narrow as $1500\,\mathrm{km\,s^{-1}}$ to be measured in an unbiased fashion, thereby pushing the accuracy of the results by almost an order of magnitude relative to backward-modelling. We thus conclude that forward-modelling observations is crucial for unbiased estimation of emission line properties from narrow-band surveys.

Appendix B: Impact of photometric redshift errors

In Sect. 4, we use spectroscopic redshift estimates to conduct SEP measurements. The J–PAS survey will soon observe hundreds of thousands of quasars for which we will only have access to photometric redshift estimates. In this section we study the impact of photometric redshift errors on SEP measurements.
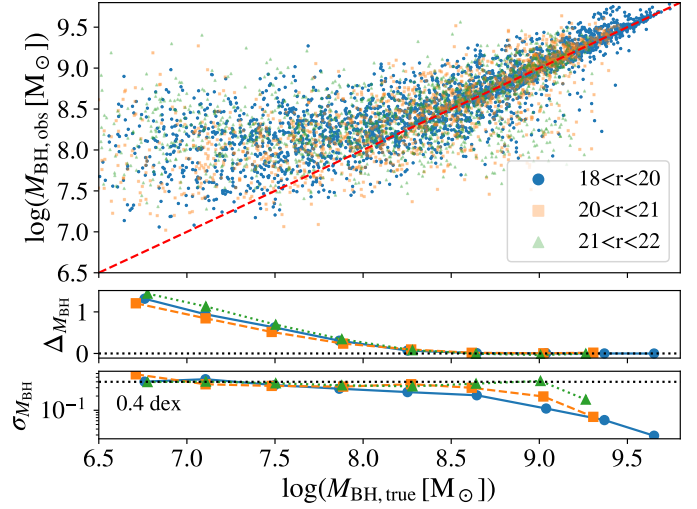
Fig. B.1. Dependence of SEP masses upon the level of photometric redshift errors expected for J–PAS quasars. Using simulated J–PAS observations, we find that the impact of these errors on SEP masses is negligible.

Forecasts for the J–PAS survey and preliminary results from the miniJPAS survey suggest that the precision of photometric redshifts for J–PAS quasars will be $\approx 0.5\%$ (Abramo et al. 2012; Chaves-Montero et al. 2017; Bonoli et al. 2021). To study the impact of this level of uncertainties on SEP results, we first perturb the actual redshift of simulated J–PAS observations (see Sect. 3.5) according to a Gaussian of width $\sigma_z = 0.005(1 + z)$, and then we apply our methodology. In Fig. B.1, we show the precision of SEP masses measured from this sample. By comparing the results shown in this figure and the lower-right panel of Fig. 3, we can readily see that the impact of photometric redshift errors on SEP masses is negligible for the level of errors expected for J–PAS.

It is important to note that the previous approach does not account for the possibility of redshift outliers, that is, sources with photometric redshift estimate very far from their actual redshift primarily due to low S/N observations and line confusion (e.g. Chaves-Montero et al. 2017). We expect minimal impact of the first type of outliers because we only analyse sources brighter than $r = 21$. On the other hand, outliers caused by line confusion are more problematic because these can be brighter than $r = 21$, and our code will return precise measurements of the misclassified line. We will carry out a more detailed study about this source of uncertainty in future works.